An Analytical Algorithm for Tensor Tomography from Projections Acquired about Three Axes

Weijie Tao, Damien Rohmer, Grant T Gullberg, Youngho Seo, Qiu Huang

An Analytical Algorithm for Tensor Tomography from Projections Acquired about Three Axes

Weijie Tao, Damien Rohmer, Grant T. Gullberg, *Life Fellow, IEEE*, Youngho Seo, *Senior Member, IEEE*, Qiu Huang, *Member, IEEE*

***Abstract*—Tensor fields are useful for modeling structure of biological tissues. The challenge to measure tensor fields involves acquiring sufficient data of scalar measurements that are physically achievable and to reconstruct tensors from as few projections as possible for efficient applications in medical imaging. In this paper, we present a filtered back-projection algorithm for the reconstruction of a symmetric second rank tensor field from directional X-ray projections about three axes. The tensor field is decomposed into a solenoidal and irrotational component each comprised of three unknowns. Using the Fourier projection theorem, a filtered back-projection algorithm is derived for the reconstruction of the solenoidal and irrotational components from projections acquired around three axes. A simple illustrative phantom consisting of two spherical shells and a 3D digital cardiac diffusion image obtained from diffusion tensor MRI of an excised human heart are used to simulate directional X-ray projections. The simulations validated the mathematical derivations and demonstrated reasonable noise properties of the algorithm. The decomposition of the tensor field into solenoidal and irrotational components provides insight into the development of algorithms for the reconstruction of tensor fields with sufficient samples in terms of the type of directional projections and the necessary orbits for acquisition of the projections of the tensor field.**

***Index Terms*— Filtered back-projection algorithm, solenoidal and irrotational components, tensor tomography, directional X-ray projections.**

I. INTRODUCTION

Tensor tomography has found important applications in the physical sciences [1, 2], mathematics [3], and medicine [4]. Here we consider the tensor tomography problem as the reconstruction of symmetric second rank tensor fields. The focus of this work is to develop acquisition schemes and filtered back-projection algorithms for the three-dimensional reconstruction of the 6-unknown tensor elements.

In medicine one application of tensors is to model biological structure by using X-ray imaging of small angle scatter to characterize in vivo fiber structure of lung [5], bone [6], and breast [7]. The small angle scattering that is captured by X-ray dark-field imaging is orientation dependent [8-15], and as such is not captured in regular 3D X-ray tomography. Thus, in many studies of X-ray dark-field imaging, the question arises as to whether sufficient data is obtained to uniquely reconstruct the tensor models used to represent the small angle scatter. Another important medical application is using tensors to model the helical fiber structure of cardiac muscle [16] using MRI diffusion imaging [17, 18]. Understanding the 3D fiber structure of the heart is important for modeling the mechanical and electrical properties; and changes in the fiber configuration may be of significant importance to understand the remodeling in the progression to heart failure [19] and after myocardial infarction [20]. Currently, most MR diffusion tensor imaging (DTI) studies require a very large number of signal measurements; whereas the focus here is to develop tensor tomographic techniques that might provide faster and more accurate data acquisitions.

The tensor tomographic problem is an extension of the vector tomographic problem [21-36] and draws on much of the work in the reconstruction of vector fields (first rank tensor fields) [31, 35]; in particular, the decomposition of the tensor field into solenoidal and irrotational components [3, 37-40] and the extension of the Fourier projection theorem from scalar and vector fields [32, 35] to tensor fields [37-40]. This decomposition provides a formulation to analyze data acquisition schemes and reconstruction algorithms from the mathematical construction of projections that might simplify the data acquisition yet provide accurate and precise reconstruction results.

The present work was stimulated by papers [41-43] where it was shown that rotations about at least three orthogonal axes are necessary to reconstruct 3D symmetric second rank tensor fields. They developed explicit plane-by-plane filtered back-projection reconstruction algorithms using six sets of projections obtained by rotating about three orthogonal axes: three sets of scalar projection measurements for diagonal components, and three for off-diagonal components. It has also been shown for slice-by-slice vector field tomography in [33, 34, 36] that three perpendicular axes are sufficient for a full

This work was supported in part by the China Scholarship Council Grant No. 201906230215 and the National Institutes of Health under Grant Nos. R43 EB027535, R01 EB026331, R01 HL135490.

W. Tao and Q. Huang are with Department of Nuclear Medicine, Rui Jin Hospital, School of Medicine, Shanghai Jiao Tong University, Shanghai, China; School of Biomedical Engineering, Shanghai Jiao Tong University, Shanghai, China (e-mail: twj2417@sjtu.edu.cn, qiuhuang@sjtu.edu.cn).

D. Rohmer is with the Geometric & Visual Computing (GeoViC) Research Team at Ecole Polytechnique/CNRS, Institut Polytechnique de Paris, 91120 Palaiseau, France (e-mail: damien.rohmer@polytechnique.edu).

G. T. Gullberg and Y. Seo are with the Department of Radiology at the University of California San Francisco 94143-0946 USA (e-mail: gtgullberg@lbl.gov, youngho.seo@ucsf.edu).

recovery. Our approach is to separate the tensor field into solenoidal and irrotational components [37-40, 44], so that one set of three directional measurements around three axes reconstructs the solenoidal component of the tensor field; and the reconstructed solenoidal component along with a different set of three directional measurements about the same axes reconstructs the irrotational component.

In the following sections, we first present definitions and notations used in our work including the formulation for the decomposition of a symmetric second rank tensor field into solenoidal and irrotational components. From this decomposition we derive a method for the reconstruction of the tensor field from measurements around three axes that involves a reconstruction of the solenoidal component, and another reconstruction of the irrotational component. In the methods we present two phantoms for evaluating the proposed algorithm. We describe how the scalar projections of the tensor fields are formed. We also present metrics used to evaluate the reconstructions and compare results with different noise levels. This is followed by a discussion of the advantages of tensor tomography.

II. Definition And Notations

In our work we use the Fourier projection theorem to show that the Fourier transform of the X-ray projections is related to the Fourier transform of the solenoidal and irrotational components of the second rank symmetric tensor field. This provides an important result proving that only a single set of directional X-ray projections around three orthogonal axes can reconstruct the solenoidal component.

A. Definition of 3D second rank tensor fields

For a point $\underline{x} = (x, y, z)^T$ in $\Re^3$, the 3D second rank tensor $T(\underline{x})$ is denoted by its nine real elements which are rapidly decreasing C$^\infty$ functions:

$$T(\underline{x}) = \begin{bmatrix} t_{xx} & t_{xy} & t_{xz} \\ t_{yx} & t_{yy} & t_{yz} \\ t_{zx} & t_{zy} & t_{zz} \end{bmatrix} (\underline{x}). \tag{1}$$

As shown in Fig. 1(a), the tensor field can be illustrated as an ellipsoid [45], where the eigenvectors $\underline{\varepsilon_1}, \underline{\varepsilon_2}, \underline{\varepsilon_3}$ of the tensor are the three unit vectors along the principal semi-axes of the ellipsoid, and the corresponding eigenvalues λ_1, λ_2, λ_3 are lengths of the principal semi-axes.

B. Fourier projection theorem for X-ray projections

In this section, we introduce the Fourier projection theorem for tensor fields, which is a straightforward extension of the Fourier slice theorem for vector fields [31, 32, 35].

Similar to the X-ray transform for a scalar image, the directional X-ray transform of a tensor field is defined here as the line integral of the tensor field along a specific direction $\underline{\theta}$ for a zenith angle θ and an azimuth angle ϕ (Fig. 1): [40]

$$p_{\underline{\theta}}^{\underline{a}\,\underline{b}}(u, v) = \int_{-\infty}^{\infty} \underline{a}^T\, T\left(t\underline{\theta} + u\underline{\alpha} + v\underline{\beta}\right) \underline{b}\, dt\,, \tag{2}$$

where the three orthogonal vectors are defined as

$$\begin{aligned} \underline{\theta} &= (sin\theta cos\phi, sin\theta sin\phi, cos\theta)^T, \\ \underline{\alpha} &= (-sin\phi, cos\phi, 0)^T, \\ \underline{\beta} &= (-cos\theta cos\phi, -cos\theta sin\phi, sin\theta)^T. \end{aligned} \tag{3}$$

Equation (2) is the directional projection measurement defined by the 3D directional unit vectors $\underline{a}$ and $\underline{b}$. In this paper, we will use directional X-ray projections measured with $\underline{a} = \underline{b} = \underline{\theta}$ and $\underline{a} = \underline{b} = \underline{\beta}$, namely $p_{\underline{\theta}}^{\underline{\theta}\,\underline{\theta}}$ and $p_{\underline{\theta}}^{\underline{\beta}\,\underline{\beta}}$. The projection $p_{\underline{\theta}}^{\underline{\theta}\,\underline{\theta}}$ indicates the integral in the direction $\underline{\theta}$ (indicated by the subscript $\underline{\theta}$) of the tensor field along the orange line presented in Fig. 1(b). The ellipsoids are a pictorial representation of the tensor at each voxel. In this case the contribution of each voxel to the line integral is the length of the orange line intersecting the ellipsoids. Whereas, for the projection $p_{\underline{\theta}}^{\underline{\beta}\,\underline{\beta}}$ presented in Fig. 1(c), the contribution of each pixel to the line integral in the direction of $\underline{\theta}$ is the length of the blue line in the direction $\underline{\beta}$ intersecting the ellipsoid.

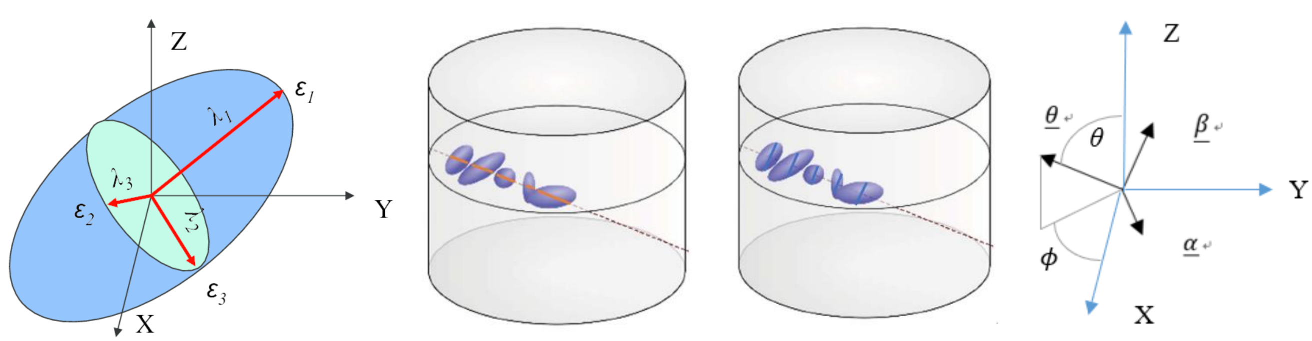

Fig. 1. (a) A second rank tensor illustrated as an ellipsoid. The eigenvectors $\underline{\varepsilon_1}, \underline{\varepsilon_2}, \underline{\varepsilon_3}$ of the tensor are the 3-unit vectors along the principal semi-axes of the ellipsoid, and the eigenvalues $\lambda_1, \lambda_2, \lambda_3$ are the lengths of the principal semi-axes. (Drawn based on Fig. 5 in [46]) (b) $p_{\underline{\theta}}^{\underline{\theta}\,\underline{\theta}}$ and (c) $p_{\underline{\theta}}^{\underline{\beta}\,\underline{\beta}}$ are the integrals along $\underline{\theta}$ of the orange intersections (along $\underline{\theta}$) and blue intersections (along $\underline{\beta}$), respectively. Here the integration line goes through the centers of all ellipsoids. (Drawn based on Fig. 5 in [46] but modified to indicate the tensor measurements along $\underline{\theta}$ and $\underline{\beta}$.) (d) Illustrations of the three orthogonal vectors $\underline{\theta}$, $\underline{\alpha}$, $\underline{\beta}$, zenith angle θ and azimuth angle ϕ.

The Fourier transform of $p_{\underline{\theta}}^{\underline{a}\,\underline{b}}(u,v)$ is defined as

$$\tilde{p}_{\underline{\theta}}^{\underline{a}\,\underline{b}}(\nu_u,\nu_v) = \int_{-\infty}^{\infty}\int_{-\infty}^{\infty} p_{\underline{\theta}}^{\underline{a}\,\underline{b}}(u,v)e^{-2\pi i(u\nu_u+v\nu_v)}\,\mathrm{d}u\mathrm{d}v. \quad (4)$$

Substituting the definition in (2) into (4), one obtains

$$\tilde{p}_{\underline{\theta}}^{\underline{a}\,\underline{b}}(\nu_u,\nu_v) = \int_{-\infty}^{\infty}\int_{-\infty}^{\infty}\int_{-\infty}^{\infty} \underline{a}^T\,T\left(t\underline{\theta}+u\underline{\alpha}+v\underline{\beta}\right)\underline{b}\,dt\,e^{-2\pi i(u\nu_u+v\nu_v)}\,\mathrm{d}u\mathrm{d}v.$$

With the change of variables $\underline{x} = t\underline{\theta}+u\underline{\alpha}+v\underline{\beta}$, it can be rewritten as

$$\tilde{p}_{\underline{\theta}}^{\underline{a}\,\underline{b}}(\nu_u,\nu_v) = \int_{-\infty}^{\infty}\int_{-\infty}^{\infty}\int_{-\infty}^{\infty} \underline{a}^T T(\underline{x})\underline{b}\,e^{-2\pi i\left(\underline{x}\underline{\alpha}\nu_u+\underline{x}\underline{\beta}\nu_v\right)}\,d\underline{x}.$$

This leads to the following formulation of the Fourier projection theorem for the projection in the direction of $\underline{\theta}$:

$$\tilde{p}_{\underline{\theta}}^{\underline{a}\,\underline{b}}(\nu_u,\nu_v) = \underline{a}^T\tilde{T}\left(\underline{\alpha}\nu_u+\underline{\beta}\nu_v\right)\underline{b} \quad (5)$$

where $\tilde{T}\left(\underline{\alpha}\nu_u+\underline{\beta}\nu_v\right)$ is the three-dimensional Fourier transform of the tensor $T(\underline{x})$ and $\underline{\alpha}\nu_u+\underline{\beta}\nu_v = \underline{\nu} = [\nu_x,\nu_y,\nu_z]^T$. We use $\tilde{}$ as the expression of the Fourier transform in the following derivation

C. Tensor field decomposition

We only consider the reconstruction of a symmetric tensor here in this work, which reduces unknown elements from 9 to 6. It was shown by Sharafutdinov [47] that any sufficiently smooth symmetric tensor field which vanishes rapidly at infinity can be decomposed in a unique way to a solenoidal component $T_\Psi^S(\underline{x})$ and an irrotational component $T_\Phi^I(\underline{x})$ (Appendix I):

$$T(\underline{x}) = T_\Psi^S(\underline{x}) + T_\Phi^I(\underline{x}), \quad (6)$$

where the solenoidal component $T_\Psi^S(\underline{x})$ is a symmetric tensor and is divergence free; and the irrotational component $T_\Phi^I(\underline{x})$ is a symmetric tensor. In (6), we specify the solenoidal component as a curl of a tensor potential in this case has to be applied to each column of Ψ (Appendix I):

$$T_\Psi^S(\underline{x}) = \nabla\times\Psi(\underline{x}), \quad (7)$$

and the tensor potential is defined as

$$\Psi(\underline{x}) = \begin{bmatrix} 0 & \frac{\partial X_1}{\partial z} & -\frac{\partial X_1}{\partial y} \\ -\frac{\partial X_2}{\partial z} & 0 & \frac{\partial X_2}{\partial x} \\ \frac{\partial X_3}{\partial y} & -\frac{\partial X_3}{\partial x} & 0 \end{bmatrix}(\underline{x}), \quad (8)$$

with three scalar functions X_1, X_2, X_3. Substituting (8) into (7), the solenoidal component is

$$T_\Psi^S(\underline{x}) = \begin{bmatrix} \frac{\partial^2 X_3}{\partial y^2}+\frac{\partial^2 X_2}{\partial z^2} & -\frac{\partial^2 X_3}{\partial y\partial x} & -\frac{\partial^2 X_2}{\partial z\partial x} \\ -\frac{\partial^2 X_3}{\partial x\partial y} & \frac{\partial^2 X_1}{\partial z^2}+\frac{\partial^2 X_3}{\partial x^2} & -\frac{\partial^2 X_1}{\partial z\partial y} \\ -\frac{\partial^2 X_2}{\partial x\partial z} & -\frac{\partial^2 X_1}{\partial y\partial z} & \frac{\partial^2 X_2}{\partial x^2}+\frac{\partial^2 X_1}{\partial y^2} \end{bmatrix}(\underline{x}). \quad (9)$$

The irrotational component in (6) is the gradient of a vector potential (Appendix I):

$$T_\Phi^I(\underline{x}) = \nabla\Phi(\underline{x}) + \left[\nabla\Phi(\underline{x})\right]^T, \quad (10)$$

and the vector potential is defined as

$$\Phi(\underline{x}) = \begin{bmatrix}\Phi_1\\ \Phi_2\\ \Phi_3\end{bmatrix}(\underline{x}), \quad (11)$$

with Φ_1, Φ_2 and Φ_3 being three scalar functions. Using (10) and (11), the irrotational component is

$$T_\Phi^I(\underline{x}) = \begin{bmatrix} 2\frac{\partial\Phi_1}{\partial x} & \frac{\partial\Phi_1}{\partial y}+\frac{\partial\Phi_2}{\partial x} & \frac{\partial\Phi_1}{\partial z}+\frac{\partial\Phi_3}{\partial x} \\ \frac{\partial\Phi_1}{\partial y}+\frac{\partial\Phi_2}{\partial x} & 2\frac{\partial\Phi_2}{\partial y} & \frac{\partial\Phi_2}{\partial z}+\frac{\partial\Phi_3}{\partial y} \\ \frac{\partial\Phi_1}{\partial z}+\frac{\partial\Phi_3}{\partial x} & \frac{\partial\Phi_2}{\partial z}+\frac{\partial\Phi_3}{\partial y} & 2\frac{\partial\Phi_3}{\partial z} \end{bmatrix}(\underline{x}). \quad (12)$$

With (9) and (12), $\tilde{T}(\underline{\nu})$ can be written in terms of the Fourier transforms of X_1, X_2, X_3, Φ_1, Φ_2 and Φ_3:

$$\tilde{T}(\underline{\nu}) = 2\pi i\begin{bmatrix} {\nu_y}^2\tilde{X}_3(\underline{\nu})+{\nu_z}^2\tilde{X}_2(\underline{\nu}) & -\nu_y\nu_x\tilde{X}_3(\underline{\nu}) & -\nu_z\nu_x\tilde{X}_2(\underline{\nu}) \\ -\nu_x\nu_y\tilde{X}_3(\underline{\nu}) & {\nu_z}^2\tilde{X}_1(\underline{\nu})+{\nu_x}^2\tilde{X}_3(\underline{\nu}) & -\nu_z\nu_y\tilde{X}_1(\underline{\nu}) \\ -\nu_x\nu_z\tilde{X}_2(\underline{\nu}) & -\nu_y\nu_z\tilde{X}_1(\underline{\nu}) & {\nu_x}^2\tilde{X}_2(\underline{\nu})+{\nu_y}^2\tilde{X}_1(\underline{\nu}) \end{bmatrix} + 2\pi i\begin{bmatrix} 2\nu_x\tilde{\Phi}_1(\underline{\nu}) & \nu_y\tilde{\Phi}_1(\underline{\nu})+\nu_x\tilde{\Phi}_2(\underline{\nu}) & \nu_z\tilde{\Phi}_1(\underline{\nu})+\nu_x\tilde{\Phi}_3(\underline{\nu}) \\ \nu_y\tilde{\Phi}_1(\underline{\nu})+\nu_x\tilde{\Phi}_2(\underline{\nu}) & 2\nu_y\tilde{\Phi}_2(\underline{\nu}) & \nu_z\tilde{\Phi}_2(\underline{\nu})+\nu_y\tilde{\Phi}_3(\underline{\nu}) \\ \nu_z\tilde{\Phi}_1(\underline{\nu})+\nu_x\tilde{\Phi}_3(\underline{\nu}) & \nu_z\tilde{\Phi}_2(\underline{\nu})+\nu_y\tilde{\Phi}_3(\underline{\nu}) & 2\nu_z\tilde{\Phi}_3(\underline{\nu}) \end{bmatrix}. \quad (13)$$

According to (6), the Fourier projection theorem in (5) becomes:

$$\tilde{p}_{\underline{\theta}}^{\underline{a}\,\underline{b}}(\nu_u,\nu_v) = \underline{a}^T\tilde{T}_\Psi^S\left(\underline{\alpha}\nu_u+\underline{\beta}\nu_v\right)\underline{b} + \underline{a}^T\tilde{T}_\Phi^I\left(\underline{\alpha}\nu_u+\underline{\beta}\nu_v\right)\underline{b}$$

Substituting (3) and (13) into the equation, we have

$$\tilde{p}_{\underline{\theta}}^{\underline{\theta}\,\underline{\theta}}(\nu_u,\nu_v) = \underline{\theta}^T\tilde{T}_\Psi^S\left(\underline{\alpha}\nu_u+\underline{\beta}\nu_v\right)\underline{\theta}, \quad (14)$$

and

$$\tilde{p}_{\underline{\theta}}^{\underline{\beta}\,\underline{\beta}}(\nu_u,\nu_v) = \underline{\beta}^T\tilde{T}_\Psi^S\left(\underline{\alpha}\nu_u+\underline{\beta}\nu_v\right)\underline{\beta} + \underline{\beta}^T\tilde{T}_\Phi^I\left(\underline{\alpha}\nu_u+\underline{\beta}\nu_v\right)\underline{\beta}. \quad (15)$$

In (14), the irrotational component $\underline{\theta}^T\tilde{T}_\Phi^I\left(\underline{\alpha}\nu_u+\underline{\beta}\nu_v\right)\underline{\theta}$ is 0.

III. ALGORITHM

We see from (14) that the directional X-ray transform $p_{\underline{\theta}}^{\underline{\theta}\,\underline{\theta}}$ is composed of only the solenoidal component, which contains the three unknowns, X_1, X_2, X_3. Thus, acquiring $p_{\underline{\theta}}^{\underline{\theta}\,\underline{\theta}}$ around three axes can be used to reconstruct the solenoidal component. Based on (15), we acquire $p_{\underline{\theta}}^{\underline{\beta}\,\underline{\beta}}$ around three axes (more than likely the same three axes), together with solutions for X_1, X_2, X_3, to reconstruct the irrotational component. This way our algorithm reconstructs the solenoidal component and the irrotational component using directional X-ray projections.

A. Solenoidal component reconstruction using $p_{\underline{\theta}}^{\underline{\theta}\,\underline{\theta}}$

In (14), the expressions for the solenoidal and irrotational components of $\tilde{p}_{\underline{\theta}}^{\underline{\theta}\,\underline{\theta}}$ are

$$\begin{aligned}\underline{\theta}^T\tilde{T}_\Psi^S\left(\underline{\alpha}\nu_u+\underline{\beta}\nu_v\right)\underline{\theta} &= (\nu_u\cos\theta\cos\phi-\nu_v\sin\phi)^2\tilde{X}_1\left(\nu_u\underline{\alpha}+\nu_v\underline{\beta}\right) \\ &\quad + \nu_u(\cos\theta\sin\phi+\nu_v\cos\phi)^2\tilde{X}_2\left(\nu_u\underline{\alpha}+\nu_v\underline{\beta}\right) \\ &\quad + (\nu_u\sin\theta)^2\tilde{X}_3\left(\nu_u\underline{\alpha}+\nu_v\underline{\beta}\right),\end{aligned} \quad (16)$$

$$\underline{\theta}^T\tilde{T}_\Phi^I\left(\underline{\alpha}\nu_u+\underline{\beta}\nu_v\right)\underline{\theta} = 0. \quad (17)$$

F(or convenience, we identify projections $p_{\underline{\theta}}^{\theta\,\theta}$ rotating about the x, y and z axes: P_x, P_y, P_z and consider reconstructing the three unknowns X_1, X_2, X_3.

For projections acquired around the x-axis, ϕ in (3) is 90°, $\underline{\theta_1}$ = (0, sinθ, cosθ), $\underline{\alpha_1}$ = (-1, 0, 0), $\underline{\beta_1}$ = (0, -cosθ, sinθ), and $[v_x, v_y, v_z]^T = v_{u_1}\underline{\alpha_1} + v_{v_1}\underline{\beta_1} = [-v_{u_1}, -v_{v_1}\cos\theta, v_{v_1}\sin\theta]^T$. Then summing (16) and (17), we have:

$$\tilde{P}_x(v_{u_1}, v_{v_1}) = {v_{v_1}}^2\tilde{X}_1\left(v_{u_1}\underline{\alpha_1} + v_{v_1}\underline{\beta_1}\right) + (v_{u_1}\cos\theta)^2\tilde{X}_2\left(v_{u_1}\underline{\alpha_1} + v_{v_1}\underline{\beta_1}\right) + (v_{u_1}\sin\theta)^2\tilde{X}_3\left(v_{u_1}\underline{\alpha_1} + v_{v_1}\underline{\beta_1}\right). \quad (18)$$

Similarly, for projections acquired around the y-axis, ϕ in (3) is 0°, $\underline{\theta_2}$= (sinθ, 0, cosθ), $\underline{\alpha_2}$=(0, 1, 0), $\underline{\beta_2}$=(-cosθ, 0, sinθ), and $[v_x, v_y, v_z]^T = v_{u_2}\underline{\alpha_2} + v_{v_2}\underline{\beta_2} = [-v_{v_2}\cos\theta, v_{u_2}, v_{v_2}\sin\theta]^T$. We can write $\tilde{p}_{\underline{\theta}}^{\theta\,\theta}$ as:

$$\tilde{P}_y(v_{u_2}, v_{v_2}) = (v_{u_2}\cos\theta)^2\tilde{X}_1\left(v_{u_2}\underline{\alpha_2} + v_{v_2}\underline{\beta_2}\right) + {v_{v_2}}^2\tilde{X}_2\left(v_{u_2}\underline{\alpha_2} + v_{v_2}\underline{\beta_2}\right) + (v_{u_2}\sin\theta)^2\tilde{X}_3\left(v_{u_2}\underline{\alpha_2} + v_{v_2}\underline{\beta_2}\right). \quad (19)$$

For $p_{\underline{\theta}}^{\theta\,\theta}$ acquired around the z-axis, θ in (3) equals 90°, $\underline{\theta_3}$= (cosϕ, sinϕ, 0), $\underline{\alpha_3}$ = (-sinϕ, cosϕ, 0), $\underline{\beta_3}$= (0, 0, 1), and $[v_x, v_y, v_z]^T = v_{u_3}\underline{\alpha_3} + v_{v_3}\underline{\beta_3} = [-v_{u_3}\sin\phi, v_{u_3}\cos\phi, v_{v_3}]^T$. We have

$$\tilde{P}_z(v_{u_3}, v_{v_3}) = (v_{v_3}\sin\phi)^2\tilde{X}_1\left(v_{u_3}\underline{\alpha_3} + v_{v_3}\underline{\beta_3}\right) + \left(v_{v_3}\cos\phi\right)^2\tilde{X}_2\left(v_{u_3}\underline{\alpha_3} + v_{v_3}\underline{\beta_3}\right) + {v_{u_3}}^2\tilde{X}_3\left(v_{u_3}\underline{\alpha_3} + v_{v_3}\underline{\beta_3}\right). \quad (20)$$

In these three equations, the zenith angle θ and the azimuth angle ϕ are not necessarily the same, neither are vectors $\underline{\alpha}$ and $\underline{\beta}$. Hence the corresponding coefficients of the vectors, v_v and v_u vary according to (18) - (20). Thus, we add numerical values of 1, 2, 3 to indicate the difference.

To solve (18) - (20) for $\tilde{X}_1$, $\tilde{X}_2$ and $\tilde{X}_3$, we need to change to the coordinate system (v_x, v_y, v_z) so that the three equations are sampled in the same 3D grid. Exchanging v_u, v_v with v_x, v_y and v_z in (18) - (20):

$$\tilde{P}_x(v_x, v_y, v_z) = \left(v_y/\cos\theta\right)^2\tilde{X}_1(v_x, v_y, v_z) + (v_x\cos\theta)^2\tilde{X}_2(v_x, v_y, v_z) + (v_x\sin\theta)^2\tilde{X}_3(v_x, v_y, v_z), \quad (21)$$

$$\tilde{P}_y(v_x, v_y, v_z) = \left(v_y\cos\theta\right)^2\tilde{X}_1(v_x, v_y, v_z) + (v_z/\sin\theta)^2\tilde{X}_2(v_x, v_y, v_z) + \left(v_y\sin\theta\right)^2\tilde{X}_3(v_x, v_y, v_z), \quad (22)$$

$$\tilde{P}_z(v_x, v_y, v_z) = (v_z\sin\phi)^2\tilde{X}_1(v_x, v_y, v_z) + (v_z\cos\phi)^2\tilde{X}_2(v_x, v_y, v_z) + (v_x/\sin\phi)^2\tilde{X}_3(v_x, v_y, v_z). \quad (23)$$

Notice that v_{v_1}, v_{v_2} and v_{u_3} have two expressions, $v_{v_1} = -v_y/\cos\theta = v_z/\sin\theta$, $v_{v_2} = -v_x/\cos\theta = v_z/\sin\theta$, $v_{u_3} = -v_x/\sin\phi = v_y/\cos\phi$. Using Cramer's rule [48] to the system of linear equations, the solutions of $\tilde{X}_1$, $\tilde{X}_2$ and $\tilde{X}_3$ are:

$$\tilde{X}_1 = \frac{(b_2c_3 - b_3c_2)\tilde{P}_x + (b_3c_1 - b_1c_3)\tilde{P}_y + (b_1c_2 - b_2c_1)\tilde{P}_z}{a_3b_1c_2 + a_2b_3c_1 + a_1b_2c_3 - a_2b_1c_3 - a_3b_2c_1 - a_1b_3c_2}, \quad (24)$$

$$\tilde{X}_2 = \frac{(a_3c_2 - a_2c_3)\tilde{P}_x + (a_1c_3 - a_3c_1)\tilde{P}_y + (a_2c_1 - a_1c_2)\tilde{P}_z}{a_3b_1c_2 + a_2b_3c_1 + a_1b_2c_3 - a_2b_1c_3 - a_3b_2c_1 - a_1b_3c_2}, \quad (25)$$

$$\tilde{X}_3 = \frac{(a_2b_3 - a_3b_2)\tilde{P}_x + (a_3b_1 - a_1b_3)\tilde{P}_y + (a_1b_2 - a_2b_1)\tilde{P}_z}{a_3b_1c_2 + a_2b_3c_1 + a_1b_2c_3 - a_2b_1c_3 - a_3b_2c_1 - a_1b_3c_2}, \quad (26)$$

where

$$a_1 = (v_y/\cos\theta)^2 = (v_z/\sin\theta)^2,\ b_1 = (v_x\cos\theta)^2,\ c_1 = (v_x\sin\theta)^2,$$
$$a_2 = (v_y\cos\theta)^2,\ b_2 = (v_z/\sin\theta)^2 = (v_x/\cos\theta)^2,\ c_2 = (v_y\sin\theta)^2,$$
$$a_3 = (v_z\sin\phi)^2,\ b_3 = (v_z\cos\phi)^2,\ c_3 = (v_x/\sin\phi)^2 = (v_y/\cos\phi)^2.$$

Once solving for $\tilde{X}_1$, $\tilde{X}_2$ and $\tilde{X}_3$, we can evaluate X_1, X_2, X_3 via the inverse Fourier transform. However, interpolating from polar to Cartesian coordinates in direct Fourier reconstruction produces angular aliasing artifacts in the reconstructed image [49]. Hence, we reconstruct X_1, X_2, X_3 slice by slice as in CT with a filtered back-projection method using an external Hamming window. Using a filtered back-projection reconstruction by filtering in frequency space or providing a convolution reconstruction in real space also suppresses high frequency noise providing smoother results.

Taking X_1 as an example, 3D inverse Fourier transform:

$$X_1(x, y, z) = \int_0^\infty\int_0^\infty\int_0^\infty \tilde{X}_1(v_x, v_y, v_z)\, e^{2\pi i(xv_x + yv_y + zv_z)} dv_x dv_y dv_z. \quad (27)$$

We transform v_x, v_y, and v_z to v_u and v_v with ϕ in (3) being 90° and arrive at

$$X_1(x, y, z) = \int_0^{2\pi}\int_0^\infty\int_0^\infty \tilde{X}_1(v_u, v_v, \theta)\, e^{2\pi i(-xv_u - yv_v\cos\theta + zv_v\sin\theta)} v_v dv_u dv_v d\theta,$$
$$= \int_0^{\pi}\int_{-\infty}^\infty\int_{-\infty}^\infty \tilde{X}_1(v_u, v_v, \theta)\, e^{2\pi i(-xv_u - yv_v\cos\theta + zv_v\sin\theta)} |v_v| dv_u dv_v d\theta. \quad (28)$$

Changing v_x, v_y and v_z to v_u and v_v, the expression of $\tilde{X}_1$ in (24) becomes

$$\tilde{X}_1(v_u, v_v, \theta) = \frac{-(v_v)^2\tilde{P}_x + (v_u\cos\theta)^2\tilde{P}_y + ((\sin\theta)^2 v_v)^2(1 + (\cos\theta)^2)\tilde{P}_z}{((\cos\theta)^3 v_u v_v)^2 + (v_v\sin\theta)^4 - (v_v\sin\theta\cos\theta)^4 - (v_v)^4}.$$

Substituting this expression for $\tilde{X}_1$:

$$X_1(x, y, z) = \int_0^{\pi}\int_{-\infty}^\infty\int_{-\infty}^\infty \frac{-(v_v)^2\tilde{P}_x + (\cos\theta v_u)^2\tilde{P}_y + ((\sin\theta)^2 v_v)^2(1 + (\cos\theta)^2)\tilde{P}_z}{((\cos\theta)^3 v_u v_v)^2 + (\sin\theta v_v)^4 - (\sin\theta\cos\theta v_v)^4 - (v_v)^4} \times e^{2\pi i(-xv_u - yv_v\cos\theta + zv_v\sin\theta)} |v_v| dv_u dv_v d\theta.$$

Let the following represent the frequency space filters multiplied by the Fourier transform of the projection components acquired about the x-, y- and z-axis:

$$\tilde{M}_x = \frac{-(v_v)^2\tilde{P}_x}{((\cos\theta)^3 v_u v_v)^2 + (\sin\theta v_v)^4 - (\sin\theta\cos\theta v_v)^4 - (v_v)^4}|v_v|,$$

$$\tilde{M}_y = \frac{(\cos\theta v_u)^2\tilde{P}_y}{((\cos\theta)^3 v_u v_v)^2 + (\sin\theta v_v)^4 - (\sin\theta\cos\theta v_v)^4 - (v_v)^4}|v_v|,$$

$$\tilde{M}_z = \frac{\left((\sin\theta)^2 v_v\right)^2(1 + (\cos\theta)^2)\tilde{P}_z}{((\cos\theta)^3 v_u v_v)^2 + (\sin\theta v_v)^4 - (\sin\theta\cos\theta v_v)^4 - (v_v)^4}|v_v|.$$

In the expressions for $\tilde{M}_x$, $\tilde{M}_y$, and $\tilde{M}_z$, we see the characteristic ramp filter $|v_v|$ multiplied by many other factors to form the filter function in our application of the algorithm.

Then applying the inverse Fourier transform, we have

$X_1(x,y,z)$ obtained by the backprojection of M_x, M_y, M_z:

$$\begin{aligned} X_1(x,y,z) = \int_0^{\pi} [&\mathrm{M}_x(-x,-y\cos\theta+z\sin\theta,\theta) \\ &+ \mathrm{M}_y(-x,-y\cos\theta+z\sin\theta,\theta) \\ &+ \mathrm{M}_z(-x,-y\cos\theta+z\sin\theta,\theta)]d\theta. \end{aligned} \quad (29)$$

Similar expressions can be derived for X_2 and X_3.

The algorithm to reconstruct the solenoidal component of the tensor field is presented below as Reconstruction 1. In the implementation, we simulate $p_{\underline{\theta}}^{\theta\,\theta}$ around x, y, z axes. Then we transform the coordinate system to keep projections around three axes the same following the Fourier transform. After transformation of the coordinate system, 2D Fourier transforms of the projections are used to calculate expressions for $\tilde{X}_1$, $\tilde{X}_2$ and $\tilde{X}_3$ in (24)-(26). At the same time, to avoid differentiation in computing the solenoidal components in the last step, we use the Fourier transform of $\partial^2 X_1/\partial z^2$ equal to $-\nu_z^2\tilde{X}_1$ in the implementation. Upon having the Fourier transform of the solenoidal components, we reconstruct each element by inverse Fourier transform and back-projection.

Reconstruction 1 Solenoidal component

Input: Directional X-ray Projections ($p_{\underline{\theta}}^{\theta\,\theta}$) P_x, P_y, P_z

for m = x, y, z **do**
  Compute $\widetilde{\mathrm{P}}_m$: Fourier transform of P_m
  Compute $\widetilde{\mathrm{M}}_m$: Filter $\widetilde{\mathrm{P}}_m$
  Compute M_m: Inverse Fourier transform of $\widetilde{\mathrm{M}}_m$
End for
for k=1, 2, 3 **do**
  Reconstruct X_k: Back-projection
end for
Compute Solenoidal component using (9)

B. Irrotational component reconstruction using $p_{\underline{\theta}}^{\beta\,\beta}$

In (14), the solenoidal and irrotational components of $\tilde{p}_{\underline{\theta}}^{\beta\,\beta}$ have the expressions as follows:

$$\begin{aligned} &\underline{\beta}^T\tilde{T}_\Psi^S\left(\underline{\alpha}\nu_u+\underline{\beta}\nu_v\right)\underline{\beta} \\ &\quad= (\nu_u\sin\theta\cos\phi)^2\tilde{X}_1\left(\nu_u\underline{\alpha}+\nu_v\underline{\beta}\right) \\ &\quad+ (\nu_u\sin\theta\sin\phi)^2\tilde{X}_2\left(\nu_u\underline{\alpha}+\nu_v\underline{\beta}\right) \\ &\quad+ (\nu_u\cos\theta)^2\tilde{X}_3\left(\nu_u\underline{\alpha}+\nu_v\underline{\beta}\right), \end{aligned} \quad (30)$$

$$\begin{aligned} &\underline{\beta}^T\tilde{T}_\Phi^I\left(\underline{\alpha}\nu_u+\underline{\beta}\nu_v\right)\underline{\beta} \\ &\quad= -2\nu_v\cos\theta\cos\phi\tilde{\Phi}_1\left(\nu_u\underline{\alpha}+\nu_v\underline{\beta}\right) \\ &\quad- 2\nu_v\cos\theta\sin\phi\tilde{\Phi}_2\left(\nu_u\underline{\alpha}+\nu_v\underline{\beta}\right) \\ &\quad+ 2\nu_v\sin\theta\,\tilde{\Phi}_3\left(\nu_u\underline{\alpha}+\nu_v\underline{\beta}\right). \end{aligned} \quad (31)$$

Similarly, we use Q_x, Q_y, Q_z to identify projections $p_{\underline{\theta}}^{\beta\,\beta}$ acquired rotating about x, y and z axes and reconstruct the three unknowns Φ_1, Φ_2 and Φ_3.

For projections acquired around the x-axis, ϕ in (3) is 90°, thus summing (30) and (31):

$$\begin{aligned} \tilde{Q}_x(\nu_{u_1},\nu_{v_1}) &= (\nu_{u_1}\sin\theta)^2\tilde{X}_2\left(\nu_{u_1}\underline{\alpha_1}+\nu_{v_1}\underline{\beta_1}\right) \\ &+ (\nu_{u_1}\cos\theta)^2\tilde{X}_3\left(\nu_{u_1}\underline{\alpha_1}+\nu_{v_1}\underline{\beta_1}\right) \\ &- 2\nu_{v_1}\cos\theta\,\tilde{\Phi}_2\left(\nu_{u_1}\underline{\alpha_1}+\nu_{v_1}\underline{\beta_1}\right) \\ &+ 2\nu_{v_1}\sin\theta\,\tilde{\Phi}_3\left(\nu_{u_1}\underline{\alpha_1}+\nu_{v_1}\underline{\beta_1}\right). \end{aligned} \quad (32)$$

For $p_{\underline{\theta}}^{\beta\,\beta}$ acquired around the y-axis, ϕ equals 0° in (3), thus:

$$\begin{aligned} \tilde{Q}_y(\nu_{u_2},\nu_{v_2}) &= (\nu_{u_2}\sin\theta)^2\tilde{X}_1\left(\nu_{u_2}\underline{\alpha_2}+\nu_{v_2}\underline{\beta_2}\right) \\ &+ (\nu_{u_2}\cos\theta)^2\tilde{X}_3\left(\nu_{u_2}\underline{\alpha_2}+\nu_{v_2}\underline{\beta_2}\right) \\ &-2\nu_{v_2}\cos\theta\,\tilde{\Phi}_1\left(\nu_{u_2}\underline{\alpha_2}+\nu_{v_2}\underline{\beta_2}\right) \\ &+ 2\nu_{v_2}\sin\theta\,\tilde{\Phi}_3\left(\nu_{u_2}\underline{\alpha_2}+\nu_{v_2}\underline{\beta_2}\right). \end{aligned} \quad (33)$$

For projections acquired around the z-axis, θ is 90° in (3), hence:

$$\begin{aligned} \tilde{Q}_z(\nu_{u_3},\nu_{v_3}) &= (\nu_{u_3}\cos\phi)^2\tilde{X}_1\left(\nu_{u_3}\underline{\alpha_3}+\nu_{v_3}\underline{\beta_3}\right) \\ &+ (\nu_{u_3}\sin\phi)^2\tilde{X}_2\left(\nu_{u_3}\underline{\alpha_3}+\nu_{v_3}\underline{\beta_3}\right) \\ &+ 2\nu_{v_3}\tilde{\Phi}_3\left(\nu_{u_3}\underline{\alpha_3}+\nu_{v_3}\underline{\beta_3}\right). \end{aligned} \quad (34)$$

Since we anticipate implementing a reconstruction where $\tilde{X}_1$, $\tilde{X}_2$ and $\tilde{X}_3$ are known as discussed in Section *A.*, we then form three equations in the three unknowns Φ_1, Φ_2 and Φ_3. Subtracting expressions for $\tilde{X}_1$, $\tilde{X}_2$ and $\tilde{X}_3$ from $\tilde{Q}_x$, $\tilde{Q}_y$ and $\tilde{Q}_z$ in (32)-(34), we arrive at the following expressions $\tilde{N}_x$, $\tilde{N}_y$ and $\tilde{N}_z$ in terms of the three unknowns Φ_1, Φ_2 and Φ_3:

$$\begin{aligned} \tilde{N}_x(\nu_{u_1},\nu_{v_1}) &= \tilde{Q}_x(\nu_{u_1},\nu_{v_1}) - (\nu_{u_1}\sin\theta)^2\tilde{X}_2\left(\nu_{u_1}\underline{\alpha_1}+\nu_{v_1}\underline{\beta_1}\right) \\ &- (\nu_{u_1}\cos\theta)^2\tilde{X}_3\left(\nu_{u_1}\underline{\alpha_1}+\nu_{v_1}\underline{\beta_1}\right), \\ &= -2\nu_{v_1}\cos\theta\,\tilde{\Phi}_2\left(\nu_{u_1}\underline{\alpha_1}+\nu_{v_1}\underline{\beta_1}\right) \\ &+ 2\nu_{v_1}\sin\theta\,\tilde{\Phi}_3\left(\nu_{u_1}\underline{\alpha_1}+\nu_{v_1}\underline{\beta_1}\right), \end{aligned} \quad (35)$$

$$\begin{aligned} \tilde{N}_y(\nu_{u_2},\nu_{v_2}) &= \tilde{Q}_y(\nu_{u_2},\nu_{v_2}) \\ &- (\nu_{u_2}\sin\theta)^2\tilde{X}_1\left(\nu_{u_2}\underline{\alpha_2}+\nu_{v_2}\underline{\beta_2}\right) \\ &- (\nu_{u_2}\cos\theta)^2\tilde{X}_3\left(\nu_{u_2}\underline{\alpha_2}+\nu_{v_2}\underline{\beta_2}\right), \\ &= -2\nu_{v_2}\cos\theta\,\tilde{\Phi}_1\left(\nu_{u_2}\underline{\alpha_2}+\nu_{v_2}\underline{\beta_2}\right) \\ &+ 2\nu_{v_2}\sin\theta\,\tilde{\Phi}_3\left(\nu_{u_2}\underline{\alpha_2}+\nu_{v_2}\underline{\beta_2}\right), \end{aligned} \quad (36)$$

$$\begin{aligned} \tilde{N}_z(\nu_{u_3},\nu_{v_3}) &= \tilde{Q}_z(\nu_{u_3},\nu_{v_3}) \\ &- (\nu_{u_3}\cos\phi)^2\tilde{X}_1\left(\nu_{u_3}\underline{\alpha_3}+\nu_{v_3}\underline{\beta_3}\right) \\ &- (\nu_{u_3}\sin\phi)^2\tilde{X}_2\left(\nu_{u_3}\underline{\alpha_3}+\nu_{v_3}\underline{\beta_3}\right), \\ &= 2\nu_{v_3}\tilde{\Phi}_3\left(\nu_{u_3}\underline{\alpha_3}+\nu_{v_3}\underline{\beta_3}\right). \end{aligned} \quad (37)$$

Likewise, to solve (35)-(37) for $\tilde{N}_x$, $\tilde{N}_y$, $\tilde{N}_z$, we change to the coordinate system (ν_x,ν_y,ν_z) by exchanging ν_u, ν_v with ν_x, ν_y and ν_z in (35) - (37):

$$\tilde{N}_x(\nu_x,\nu_y,\nu_z) = 2\nu_y\tilde{\Phi}_2(\nu_x,\nu_y,\nu_z) + 2\nu_z\tilde{\Phi}_3(\nu_x,\nu_y,\nu_z) \quad (38)$$

$$\tilde{N}_y(\nu_x,\nu_y,\nu_z) = 2\nu_x\tilde{\Phi}_1(\nu_x,\nu_y,\nu_z) + 2\nu_z\tilde{\Phi}_3(\nu_x,\nu_y,\nu_z) \quad (39)$$

$$\tilde{N}_z(\nu_x,\nu_y,\nu_z) = 2\nu_z\tilde{\Phi}_3(\nu_x,\nu_y,\nu_z) \quad (40)$$

After coordinate system transformation, the solutions of $\tilde{\Phi}_1$, $\tilde{\Phi}_2$ and $\tilde{\Phi}_3$ are:

$$\tilde{\Phi}_1 = \frac{\tilde{N}_y - \tilde{N}_z}{2\nu_x} \quad (41)$$

$$\tilde{\Phi}_2 = \frac{\tilde{N}_x - \tilde{N}_z}{2\nu_y} \tag{42}$$

$$\tilde{\Phi}_3 = \frac{\tilde{N}_z}{2\nu_z} \tag{43}$$

Like the reconstruction of X_1, we reconstruct Φ_1 with projections around the x-axis. Exchanging ν_x, ν_y and ν_z to ν_u, ν_v in (41)

$$\tilde{\Phi}_1 = \frac{\tilde{N}_y - \tilde{N}_z}{-2\nu_u}. \tag{44}$$

The 3D inverse Fourier transform of $\tilde{\Phi}_1$ is

$$\Phi_1(x,y,z) = \int_0^{\infty}\int_0^{\infty}\int_0^{\infty} \tilde{\Phi}_1(\nu_x,\nu_y,\nu_z)\, e^{2\pi i(x\nu_x + y\nu_y + z\nu_z)} d\nu_x d\nu_y d\nu_z.$$

We transform ν_x, ν_y and ν_z to ν_u and ν_v:

$$\Phi_1(x,y,z) = \int_0^{2\pi}\int_0^{\infty}\int_0^{\infty} \tilde{\Phi}_1(\nu_u,\nu_v,\theta)\, e^{2\pi i(-x\nu_u - y\nu_v\cos\theta + z\nu_v\sin\theta)} \nu_v d\nu_u d\nu_v d\theta\,.$$

Substituting the expression for $\tilde{\Phi}_1$:

$$\begin{aligned}\Phi_1(x,y,z) &= -\int_0^{2\pi}\int_0^{\infty}\int_0^{\infty} \frac{\tilde{N}_y - \tilde{N}_z}{2\nu_u} e^{2\pi i(-x\nu_u - y\nu_v\cos\theta + z\nu_v\sin\theta)} \nu_v d\nu_u d\nu_v d\theta \\ &= -\int_0^{\pi}\int_{-\infty}^{\infty}\int_{-\infty}^{\infty} \frac{\tilde{N}_y - \tilde{N}_z}{2|\nu_u|} e^{2\pi i(-x\nu_u - y\nu_v\cos\theta + z\nu_v\sin\theta)} |\nu_v| d\nu_u d\nu_v d\theta. \end{aligned} \tag{45}$$

Let $\tilde{L}_y = \frac{\tilde{N}_y}{2|\nu_u|}|\nu_v|$ and $\tilde{L}_z = \frac{\tilde{N}_z}{2|\nu_u|}|\nu_v|$, then taking the inverse Fourier transform, we have $\Phi_1(x,y,z)$ obtained by the backprojection of L_y and L_z:

$$\begin{aligned}\Phi_1(x,y,z) = \int_0^{\pi} [&L_y(-x, -ycos\theta + zsin\theta, \theta) \\ &- L_z(-x, -ycos\theta + zsin\theta, \theta)] d\theta. \end{aligned} \tag{46}$$

Φ_2 and Φ_3 can be derived similarly.

The algorithm to reconstruct the irrotational component of the tensor field is presented below as Reconstruction 2. We also implement a hamming window in the filtered backprojection method based on the expressions for Φ_1, Φ_2 and Φ_3. The implementation to reconstruct the irrotational component is the same as that for solenoidal component in Reconstruction 1.

Reconstruction 2 Irrotational component

Input: Directional X-ray Projections $(p_{\theta}^{\beta\beta})$ Q_x, Q_y, Q_z

for m = x, y, z **do**

  Compute $\tilde{Q}_m$:Fourier transform of Q_m

  Compute $\tilde{N}_m$: Merging $\tilde{Q}_m$ and $\tilde{X}_1$, $\tilde{X}_2$, $\tilde{X}_3$

  Compute $\tilde{L}_m$: Filter $\tilde{N}_m$

  Compute L_m: Inverse Fourier transform of $\tilde{L}_m$

End for

for k=1, 2, 3 **do**

  Reconstruct Φ_k: Back-projection

end for

Compute Irrotational component using (12)

IV. Methods

The following presents the methods used to evaluate our algorithm. In particular we used two phantoms, one a discrete numerical phantom and the other a realistic diffusion tensor field of an excised human heart.

A. Discrete representation of the tensor field

The discretized tensor field is stored as a $9N^3$ matrix, containing the nine elements of the second rank tensor field for each voxel of an N × N × N voxel grid. Projection data are represented by a 3 × n_θ × h × w matrix, where for each 3 rotation axes (X, Y and Z axes), h × w tomographic projections are acquired at n_θ angular steps with h being the number of two-dimensional slices and w being radius of rotation.

B. Phantoms

1) A simple illustrative phantom

The first phantom was constructed using (9) and (12) from two balls of uniform intensities placed in a 128 × 128 × 128 array as shown in Fig. 2(a). Six 128 × 128 × 128 arrays were assembled, such that in each array the two balls took on one of the scalar values for X_1, X_2, X_3, Φ_1, Φ_2 and Φ_3 in Fig. 2(b). Thus, each array had two balls with the same constant value and a uniform background. Using gradient as shown in (9) and (12), solenoidal and irrotational components were generated separately, and then summed to obtain the tensor field for the phantom. The generated solenoidal, irrotational components and tensor field only contains the borders of the ball, other area is 0. Fig. 3 (a), (b), (c) display the x-y slice through the center of the 9 elements for the solenoidal component, the irrotational component, and the sum forming the tensor field for the phantom, respectively.

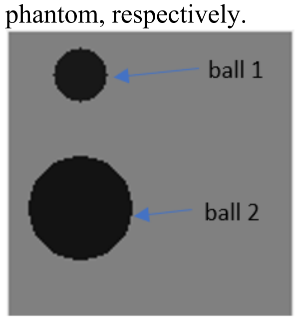

	ball 1	ball 2	background
X_1	19	15	100
X_2	12	32	130
X_3	10.3	10	113
Φ_1	6.9	19	31
Φ_2	15	15	44
Φ_3	16	26	53

(a) (b)

Fig. 2. Six scalar fields were used to form the tensor field using (9) and (12). (a) Illustration of the central transaxial slice through the two balls that were assigned the scalar values in the table (b) for the tensor potential (X_1, X_2, X_3) and the vector potential (Φ_1, Φ_2, Φ_3).

2) Cardiac diffusion tensor image

The second phantom used for simulations in this work is a cardiac diffusion tensor image that was obtained by scanning a normal excised human heart with a 4-element phased array coil on a 1.5 T GE CV/I MRI Scanner (GE Medical System, Waukesha, WI). Details about the heart and acquisition parameters are described in [50].

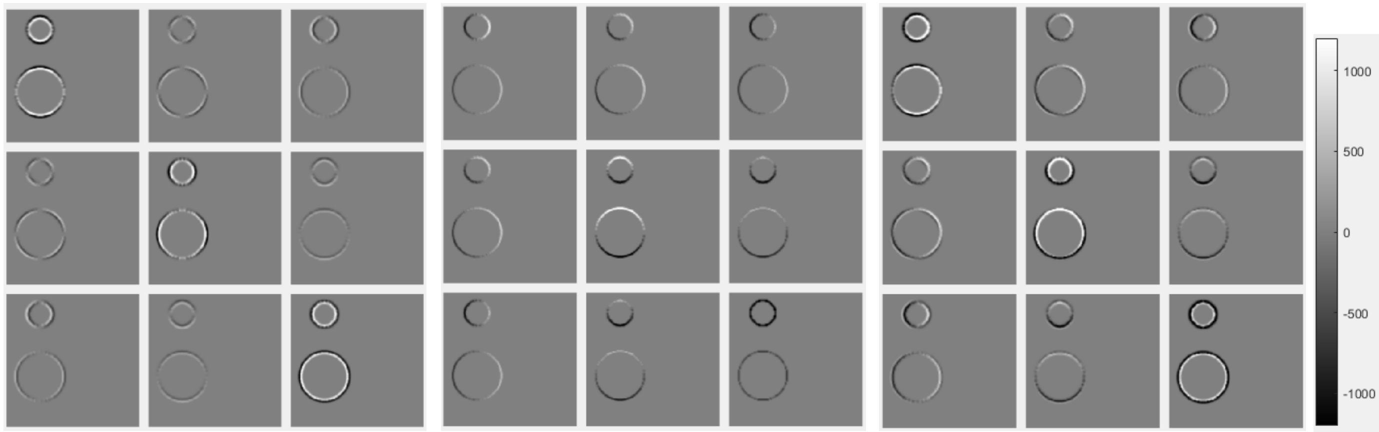

(a) (b) (c)

Fig. 3. The x-y slice through the center of the 9 elements for (a) solenoidal component, (b) irrotational component and (c) tensor field

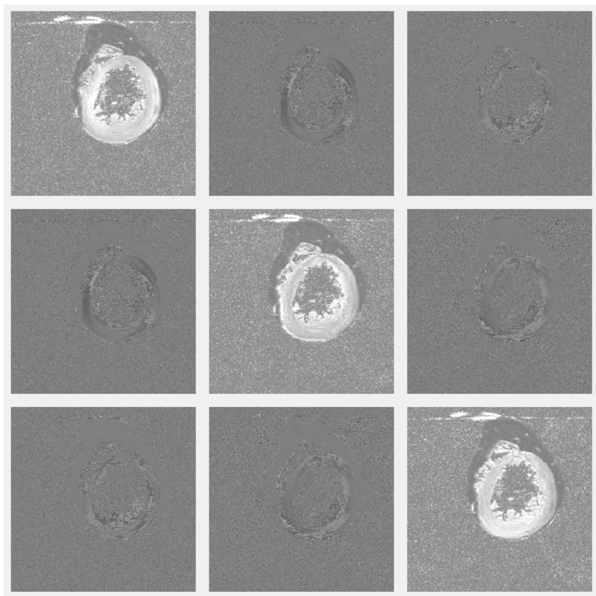

Fig. 4. Nine elements of cardiac diffusion tensor phantom

The diffusion tensor T was obtained from [14] as eigenvectors $\underline{\varepsilon}_1$, $\underline{\varepsilon}_2$ and $\underline{\varepsilon}_3$ with eigenvalues λ_1, λ_2 and λ_3 for $\lambda_1 \geq \lambda_2 \geq \lambda_3$. The data set was arranged in a 256 × 256 × 134 array for each eigenvector and eigenvalue, with voxel size being 429.7 µm × 429.7 µm ×1000 µm. Denoting V as the matrix of eigenvectors and D = diag (λ_1, λ_2, λ_3) as the diagonal matrix of eigenvalues, the diffusion tensor can be computed from $T = VDV^T$. The 9 elements of the cardiac diffusion tensor phantom are shown in Fig. 4, which were reformulated from the eigenvalues and eigenvectors.

C. Forward model

We used the same method to generate the projections for the simple numerical phantom and the heart diffusion tensor field calculated using the eigenvectors and eigenvalues. Both the phantom and projections had the same pixel size. A discrete version of the scalar projections $p_{\underline{\theta}}^{\underline{\theta}\,\underline{\theta}}$ and $p_{\underline{\theta}}^{\underline{\beta}\,\underline{\beta}}$ were formed using ray tracing. For example, taking $p_{\underline{\theta}}^{\underline{\theta}\,\underline{\theta}}$ acquired around the x-axis, ϕ in (3) is 90° and $\underline{\theta}$ = (0, $sin\theta$, $cos\theta$). Due to symmetry, t_{yz} is the same as t_{zy}. Our approach generates each projection one angle (one θ value in this example) at a time for the directional X-ray transform

$$p_{\underline{\theta}}^{\underline{\theta}\,\underline{\theta}} = \int_{-\infty}^{\infty} \underline{\theta}^T\, T\left(t\underline{\theta} + u\underline{\alpha} + v\underline{\beta}\right)\underline{\theta}\, dt$$

$$= \int_{-\infty}^{\infty} \left(t_{yy}sin^2\theta\ + 2t_{yz}sin\theta cos\theta + t_{zz}cos^2\theta\right)dt.$$

Using ray-tracing, the contribution of each voxel to the integral was calculated by multiplying the length of the voxel intersection with the ray multiplied by the value of the tensor elements (t_{yy}, t_{yz} and t_{zz}) times their coefficients ($sin^2\theta$, $2sin\theta cos\theta$ and $cos^2\theta$) in the voxel. For each of the three rotation axes, the phantom rotated through 180° in 1° increments so that a total of 540 parallel projections were formed about three axes.

D. Evaluation

To evaluate the difference between the reconstruction results and the phantom, we used the 2-norm error by summing the normalized difference between the reconstruction and phantom for each tensor element and for each first principal eigenvalue as given by the following expressions for the tensors and principal eigenvalues, respectively:

$$S_t(T_{uv}) = \frac{\sum_{i=1}^{N}\left(\frac{Recon_{T_{uv}^i} - Phantom_{T_{uv}^i}}{\max\limits_{k=1,\cdots,N}\left(Phantom_{T_{uv}^k}\right) - \min\limits_{k=1,\cdots,N}\left(Phantom_{T_{uv}^k}\right)}\right)^2}{N} \tag{47}$$

$$S_e(E_{11}) = \frac{\sum_{i=1}^{N}\left(\frac{Recon_{E_{11}^i} - Phantom_{E_{11}^i}}{\max\limits_{k=1,\cdots,N}\left(Phantom_{E_{11}^k}\right) - \min\limits_{k=1,\cdots,N}\left(Phantom_{E_{11}^k}\right)}\right)^2}{N} \tag{48}$$

where N is the number of voxels that at summed over; $Recon_{T_{uv}^i}$ is the value in voxel i of the reconstructed tensor element T_{uv}^i and $Phantom_{T_{uv}^i}$ is the value in voxel i of the phantom tensor element T_{uv}^i ; and $Recon_{E_{11}^i}$ is the value in voxel i of the reconstructed tensor element principal eigenvalue E_{11}^i and $Phantom_{E_{11}^i}$ is the value in voxel i of the phantom tensor element principal eigenvalue E_{11}^i.

Fractional anisotropy (FA) was also used to deduce the accuracy of the reconstructions. FA gives the degree of anisotropy of a diffusion process and is defined using the eigenvalues (λ_1, λ_2 and λ_3) of the tensor:

$$\mathrm{FA} = \sqrt{\frac{3}{2}}\frac{\sqrt{(\lambda_1-\lambda)^2+(\lambda_2-\lambda)^2+(\lambda_3-\lambda)^2}}{\sqrt{\lambda_1^2+\lambda_2^2+\lambda_3^2}} \tag{49}$$

where $\lambda = \frac{\lambda_1+\lambda_2+\lambda_3}{3}$.

To evaluate the noise property of the algorithm, we calculated the signal-to-noise ratio (SNR) for the first principal eigenvalue of the reconstructions, which is defined:

$$SNR = \frac{Recon_{E_{11}}}{\sigma_{E_{11}}} \tag{50}$$

where $Recon_{E_{11}}$ and $\sigma_{E_{11}}$ are the mean and the standard deviation of the reconstructed tensor principal eigenvalue E_{11}, respectively.

V. Results

A. A simple illustrative phantom

1) Solenoidal component

The reconstruction through the center slice of the solenoidal component for the simulated tensor field of the simple illustrative phantom is displayed element by element in Fig. 5. We reconstructed the projections $p_{\underline{\theta}}^{\theta\,\theta}$ acquired around three axes using the method in Reconstruction 1. The reconstructed image matrix was 128 × 128 × 128, the same as that of the phantom. The three columns from left to right form the nine elements of the phantom (as defined in Fig. 3(a)), the reconstructed image, and their profiles along the red line in the first column in Fig. 5(a). The profiles of the reconstructed image are similar to those of the phantom. The central slice of the numerical phantom was selected to evaluate the quantitative accuracy of our algorithm using S_t in (47). Table 1 summarizes the results for each tensor element. Due to symmetry of the tensor, T_{xy} and T_{yx} have the same S_t, so does T_{xz} and T_{zx}; and T_{yz} and T_{zy}. From the table, the errors in the reconstructed solenoidal component are small (< 0.0008).

Table 1. The S_t for each element of the solenoidal component, irrotational component and tensor field for the simple illustrative phantom

	solenoidal component	irrotational component	tensor field
T_{xx}	7.4057e-5	2.0640e-4	2.4870e-4
T_{xy}/T_{yx}	3.1368e-4	1.0679e-3	8.5493e-4
T_{xz}/T_{zx}	5.1750e-4	6.9623e-4	6.3424e-4
T_{yy}	8.4666e-5	5.2978e-4	7.2026e-4
T_{yz}/T_{zy}	7.3759e-4	2.2040e-4	2.2134e-3
T_{zz}	3.8806e-4	3.1039e-4	1.5316e-3

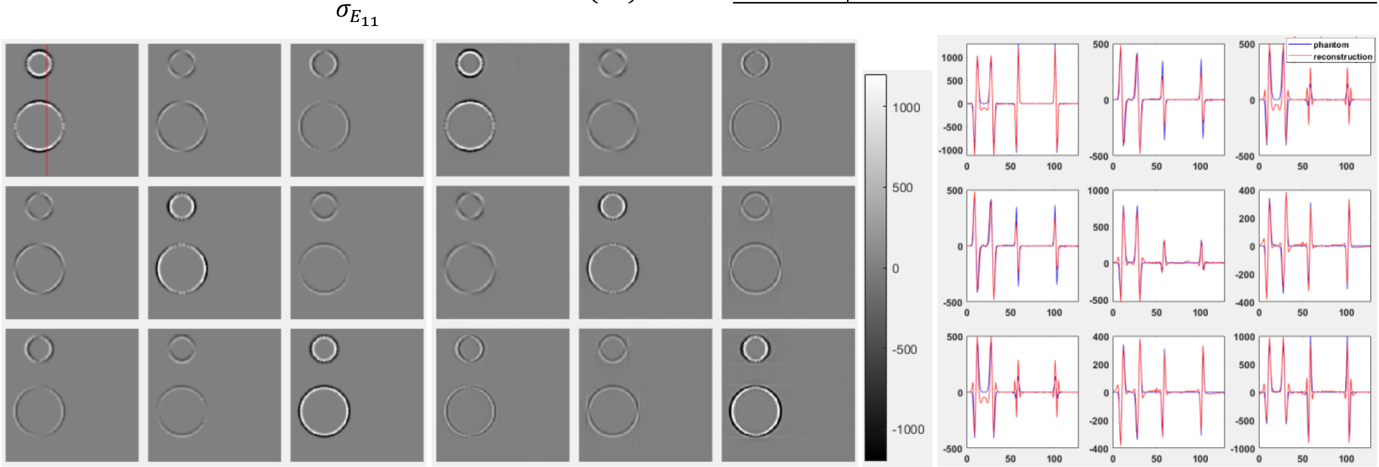

(a) (b) (c)

Fig. 5. Reconstruction of the solenoidal component of the phantom. (a) The x-y slice through the center of the 9 elements of the phantom, (b) The x-y slice through the center of the 9 elements of the reconstructed image, (c) Profiles in each element along the red line as example in (a).

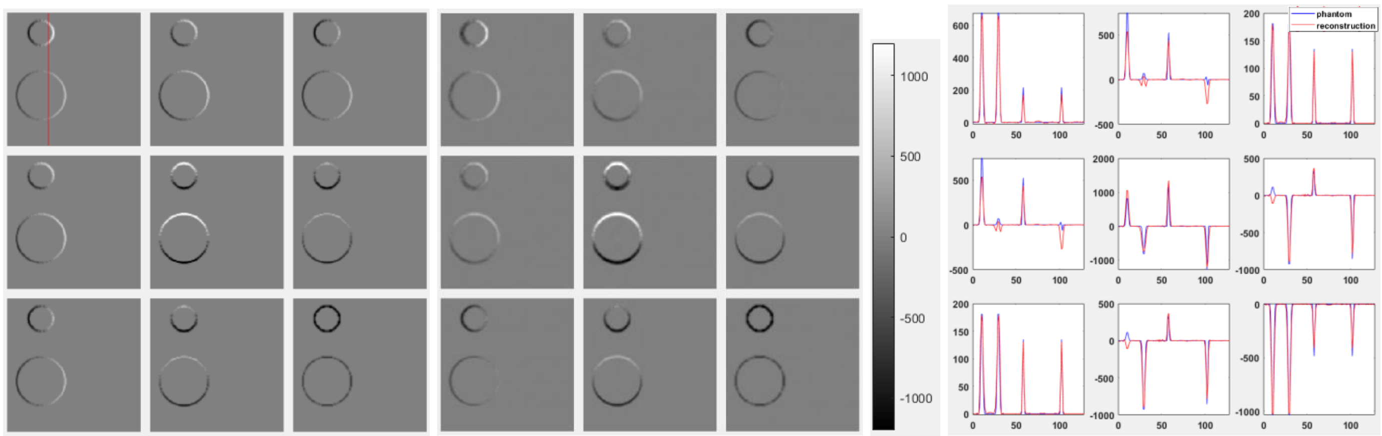

(a) (b) (c)

Fig. 6. Reconstruction of the irrotational component of the phantom. (a) The x-y slice through the center of the 9 elements of the phantom, (b) The x-y slice through the center of the 9 elements of the reconstructed image, (c) Profiles in each element along the red line as example in (a).

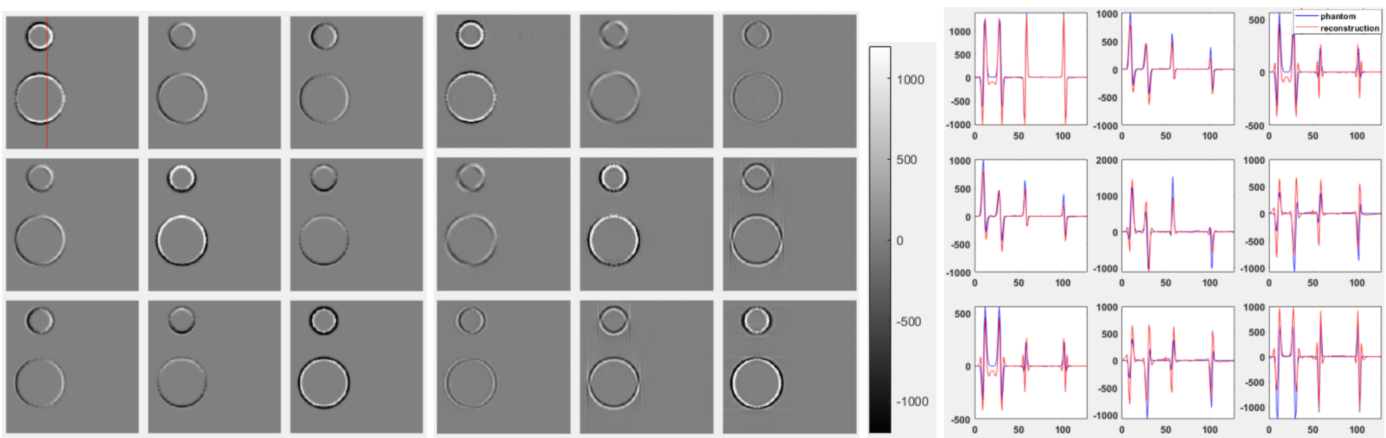

(a) (b) (c)

Fig. 7. Reconstruction of the tensor field of the phantom [solenoidal + irrotational]. (a) The x-y slice through the center of the 9 elements of the phantom, (b) The x-y slice through the center of the 9 elements of the reconstructed image, (c) Profiles in each element along the red line as example in (a).

2) Irrotational component

Fig. 6 presents each element of the estimates through the center slice of the irrotational component for the simulated phantom. The projections $p_{\underline{\theta}}^{\beta\beta}$ acquired around three axes were reconstructed following the steps in Reconstruction 2. Profiles in Fig. 6 indicate the similarity between the reconstructed images and the phantom. We calculated the S_t for each reconstructed element of the reconstructions as listed in Table 1. The errors are small but mostly larger than those for the solenoidal component.

3) Tensor field

The reconstruction of the tensor field is obtained by summing the solenoidal component and the irrotational component. The x-y slice through the center of the 9 elements of the reconstructions together with that of the phantom are given in Fig. 7. Some Gibbs artifacts are in the profiles because of the sharp frequency filters. The quantitative results in table 1 show that the errors for the reconstructed tensor field are small but generally larger than each of its solenoidal and irrotational components, except for T_{xy}/T_{yx} and T_{xz}/T_{zx}.

B. Cardiac diffusion tensor image

The solenoidal and irrotational component of the cardiac diffusion tensor field with image matrix size of 256 × 256 × 256 were estimated from simulated projections with Gaussian noise added. The Gaussian noise are with zero mean and two different standard derivations (0.01 and 0.02). Summing the reconstructed solenoidal and irrotational components resulted in the complete tensor field. The reconstructions were then transformed into a matrix formulation of the eigenvalues and eigenvectors. The first principal eigenvalues for three slices are shown in Fig. 8 and the S_e in (48) are listed in table 2. Fig. 9 gives the FA [calculated from (49)] for the same three slices. Also, table 3 lists SNR results [calculated from (50)] for the reconstructed tensor first principal eigenvalues. In each slice, we chose a relatively uniform region of interest to calculate the SNR, which has a value range from 1.6565 to 2.5343. We can see more degradation in the image quality with higher noise level.

Slice 78

Slice 128

Slice 160

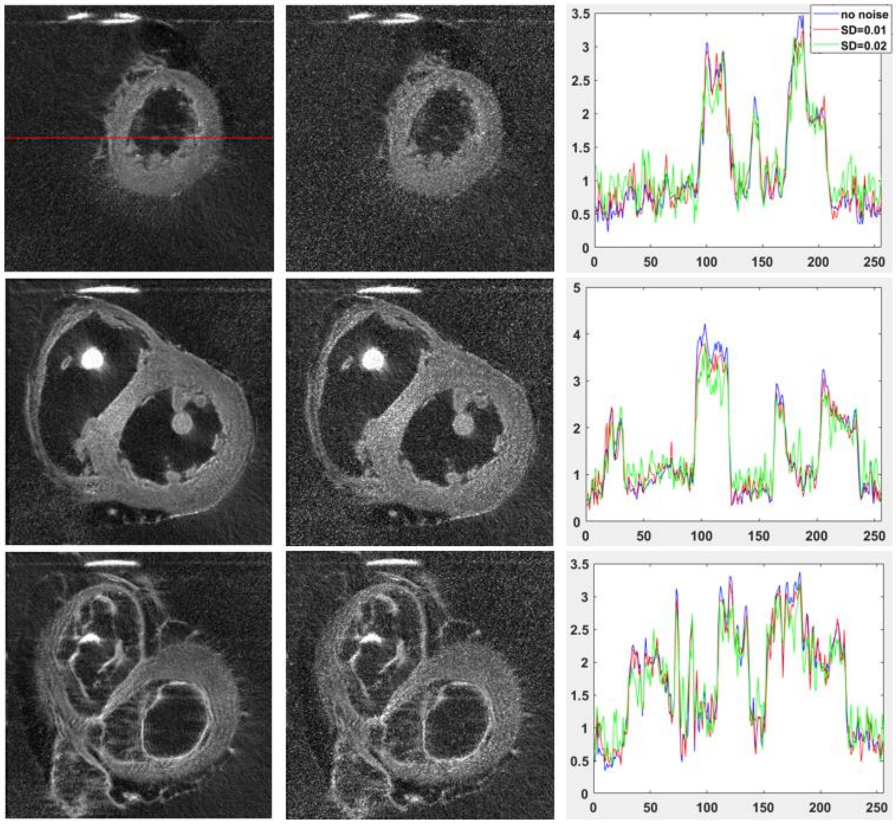

Fig. 8. First principal eigenvalue of reconstructed image with Gaussian noise SD = 0.01 [solenoidal + irrotational] (left); reconstructed image with Gaussian noise SD = 0.02 [solenoidal + irrotational] (middle); and profiles along the red line (right). The series of images from top to bottom are slice 78, slice 128, slice 160, respectively.

Slice 78

Slice 128

Slice 160

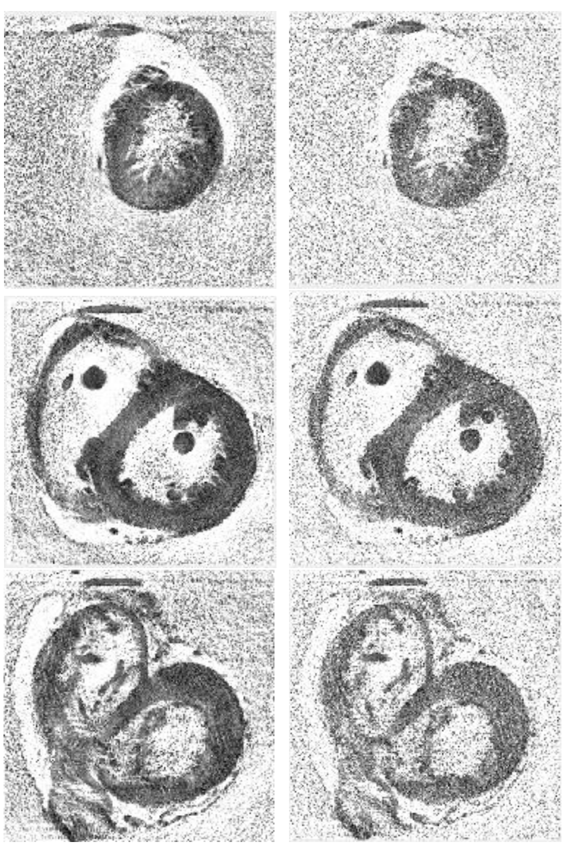

Fig. 9. FA of reconstructed image with Gaussian noise SD = 0.01 (left); reconstructed image with Gaussian noise SD = 0.02 (right). The series of images from top to bottom are slice 78, slice 128, slice 160, respectively.

Table 2. The S_e for first principal eigenvalues of the cardiac diffusion tensor phantom

	No noise	SD=0.01	SD=0.02
Slice 78	0.0017	0.0020	0.0033
Slice 128	0.0017	0.0025	0.0049
Slice 160	0.0026	0.0031	0.0058

Table 3.SNR for the first principal eigenvalues of the cardiac diffusion tensor phantom

	No noise	SD=0.01	SD=0.02
Slice 78	21.86	16.71	10.96
Slice 128	22.95	17.73	13.25
Slice 160	15.09	12.73	8.75

VI. Discussion

This study provides the derivation of a new filtered back-projection algorithm for the reconstruction of tensor fields from data acquired about three axes. The tensor field is decomposed into solenoidal and irrotational components, both of which have three unknown elements. Fourier projection theorem provides relationships between the Fourier transform of the directional X-ray projections and the Fourier transform of the solenoidal and irrotational components of the tensor field [37-40]. In solving for the three unknowns in the solenoidal and irrotational component, new filters are formed involving coefficients of three equations times the characteristic ramp filter [see expressions before (29) and (46)]. Different from previous work acquiring projections about at least six [51] or three orthogonal axes [43], our proposed algorithm provides the possibility for using projections about three axes to solve the unknowns of the solenoidal and irrotational component separately. The three axes for acquiring projections $p_{\underline{\theta}}^{\underline{\theta}\,\underline{\theta}}$ for the solenoidal component are the same as the three axes for acquiring projections $p_{\underline{\theta}}^{\underline{\beta}\,\underline{\beta}}$ for the irrotational component. All derived formulas lead to an analytical reconstruction algorithm for tensor field from projections acquired about three axes.

A. Summary of results

The proposed algorithm provides estimates of a total of 6 unknowns, 3 for the solenoidal and 3 for the irrotational component of the tensor field. Two phantoms were used to evaluate our algorithm. One was a numerical phantom with no special imaging modality in mind from which we could test our algorithm. Potential values were assigned to the solenoidal and irrotational components. The calculation of the partial derivatives formed tensor elements with two spherical surfaces with interior and background equal to zero. We choose the particular tensor field to evaluate the algorithm performance; in particular, to evaluate the algorithm performance of potential Gibbs artifacts at sharp boundaries. If one wants to interpret the phantom for a particular imaging modality, such as X-ray dark field imaging, one might construe the phantom to be two spherical surfaces that are imbedded in a uniform background of material with microstructure having anisotropic small angle scatter at the boundary of the surfaces but virtually no anisotropic small angle scatter in the background material, only isotropic scatter that attenuates the signal with no anisotropic structure. We see in Fig. 5-7 that the algorithm gives reconstructed results, where at the boundary of the spherical surfaces there are undershoots and overshoots of reconstructed values compared to the original phantom values. The second phantom was a cardiac diffusion tensor field that was obtained by scanning a normal excised human heart on a 1.5 T GE CV/I MRI Scanner (GE Medical System, Waukesha, WI). Transforming the tensor matrix to its diagonal form provides a singular value decomposition with singular values (eigenvalues), which specify the principal eigenvector with potentially positive and negative elements that one could consider in the first phantom provide the principal direction of the scatter and in the second phantom provide the principal direction of the diffusion relative to the Cartesian coordinate system in Fig. 1. In Fig. 8 the eigenvalues, determined from the reconstructed tensor field of the cardiac diffusion tensor phantom, have larger errors in the reconstruction when noise is added to the projections. These errors are demonstrated better in the FA images in Fig. 9. Our calculations of the signal to noise ratio (SNR) for the first principal eigenvalues (table 3) ranged between 9 and 18, which is low but in line with what one would expect in a single MR-DTI with typical values of 15:1 to 30:1 [52]. It is likely that the noise in the original cardiac tensor image is amplified with the addition of noise in the projections as shown in table 2.

B. X-ray and Radon projections of tensor fields

Our work in this paper focused on developing a filtered backprojection algorithm for reconstructing longitudinal and transverse X-ray projections, in the same way reconstruction algorithms can be developed for Radon projections of second rank tensor fields [36, 40, 44, 53-55]. To illustrate the differences between X-ray and Radon projections, let $\underline{x} = (x, y, z)$ be a point in $\Re^3$ and let the components $t_{ij}(\underline{x})$ of a second rank symmetric tensor field $T(\underline{x})$ be real, rapidly decreasing C^∞ functions defined on $\Re^3$. For the tensor field $T(\underline{x})$, the 3D directional X-ray transform of $T(\underline{x})$ is defined by $p_{\underline{\theta}}^{\underline{a}\,\underline{b}}(\underline{s};\underline{\theta}) = \int_{\Re} \underline{a}^T T(\underline{s} + l\underline{\theta})\underline{b}\, dl$, and the 3D directional Radon transformation of $T(\underline{x})$ is defined by $r_{\underline{\theta}}^{\underline{a}\,\underline{b}}(t;\underline{\theta}) = \int_{\Re^3} \underline{a}^T T(\underline{x})\underline{b}\delta(\underline{x}\cdot\underline{\theta} - t)d\underline{x}$. These are scalar projection measurements in the direction of $\underline{\theta}$ formed by the product of the tensor T with the three-dimensional unit vectors $\underline{a}$ and $\underline{b}$. For this work we focus primarily on the X-ray scalar projection measurements of the tensor field for vectors $\underline{a}$ and $\underline{b}$ equal to combinations of the orthogonal vectors $\underline{\theta} = (sin\theta cos\phi, sin\theta sin\phi, cos\theta)^T$, $\underline{\alpha} = (-sin\phi, cos\phi, 0)^T$ and $\underline{\beta} = (-cos\theta cos\phi, -cos\theta sin\phi, sin\theta)^T$ in developing a filtered backprojection reconstruction algorithm. In this paper we demonstrate that there is indeed a reconstruction algorithm for transvers reconstruction tomography for a general tensor field using data from only three rotation axes. The method first performs a slice-by-slice reconstruction of six functions by two-dimensional backprojection and filter methods. The components of tensor field are related to these functions by a linear operator with coefficients that are rational functions of the Fourier transform variables.

C. Solution for three orthogonal axes

It has been shown in other work [42, 55] that three orthogonal chosen directions are sufficient for reconstruction of a tensor field. It has also been shown [33, 34, 36] that three orthogonal axes are sufficient for a full recovery of a vector field from slice-by-slice vector field tomography. In [33] an efficient mollifier method was proposed for three-dimensional vector tomography problem. The mollifier method originally proposed by Louis in 1990 [56] is seen throughout his group's work [35, 36, 44] and provides an approximate solution to a continuous inverse problem which one might see very similar to the determination of a regularized solution in the implementation of discrete Bayesian reconstruction methods. For the tensor tomography problem there is the longitudinal projection in additional to a transverse projection [34, 43] needed for every projection angle to solve for the 6 unknown tensor elements, whereas only one longitudinal projection for each angle is required for the vector tomography problem. For stability it is proposed that 3 orthogonal axes are needed to recover vector fields and 6 orthogonal axes are needed to recover tensor fields [34]. Different from these works, our filtered backprojection algorithm uses longitudinal and transverse projections about three orthogonal axes to solve the unknowns of the solenoidal and irrotational component separately.

D. Helmholtz decomposition

1) Unbounded domains

It was shown by Sharafutdinov in [47], that a smooth symmetric tensor field which vanishes rapidly at infinity can be decomposed in a unique way as $t_{ij}(\underline{x}) = t_{ij}^S(\underline{x}) + \frac{1}{2}(\partial_i \varphi_j(\underline{x}) + \partial_j \varphi_i(\underline{x}))$ where $\underline{\varphi}(\underline{x})$ is a vector potential and $T_S(\underline{x})$ is a symmetric solenoidal tensor field, which is divergence free: $\sum_i \partial_i t_{ij}^S(\underline{x}) = \sum_j \partial_j t_{ij}^S(\underline{x}) = 0$. Here we considered a similar decomposition of a symmetric tensor field T: $T(\underline{x}) = T_\Psi^S(\underline{x}) + T_\Phi^I(\underline{x})$, where the symmetric divergent-free solenoidal component $T_\Psi^S(\underline{x})$ is the curl of a tensor potential, $T_\Psi^S(\underline{x}) = \nabla \times \Psi(\underline{x})$, and the symmetric irrotational component $T_\Phi^I(\underline{x})$ is the gradient of a vector potential, $T_\Phi^I(\underline{x}) = \nabla\Phi(\underline{x}) + [\nabla\Phi(\underline{x})]^T$ [37]. This formulation provides a parameterization of the solenoidal and irrotational components each by three scalar functions [(9), (12), and Appendix]. This combines the results of Sharafutdinov [47] with that of the Helmholtz decomposition [57] for vector fields where the solenoidal component is the curl of a vector potential and the irrotational component is the gradient of a scalar potential. We showed in this paper a solution for the solenoidal and irrotational components involves a reconstruction using the Fourier filter backprojection algorithm. Another example of decomposing tensor fields into solenoidal and irrotational components to solve for both the tensor elements and potentials is presented in [44]. A solution on general differential manifolds is presented in [41] providing an explicit inverse formula for reconstruction of the solenoidal component of a second rank tensor field from projections acquired about three axes. Different from these decompositions is the singular value decomposition of a dynamic acquisition of 2-tensors in $\mathbb{R}^2$ used to solve the inverse of the dynamic tensor projections [58]. This is to our knowledge the first application of tensor tomography to a dynamic acquisition of tensor projections.

2) Bounded domains

The application of our algorithm to bounded domains is an interesting study. The early work related to vector field tomography on bounded domains resulted in several papers [22, 24, 25, 59]. Specifically, Braun and Hauck [24] recognized that bounded domains admit harmonic vector fields that are both irrotational and solenoidal. Therefore, the decomposition into irrotational and solenoidal components is not unique. In their paper, they proposed that the decomposition should be $V = V^S + V^I + V_H$, where $V^S = \nabla \times \Psi$, $V^I = \nabla\Phi$, and V_H is the harmonic component of the vector field satisfying $\nabla^T V_H = 0$ and $\nabla \times V_H = 0$. The solenoidal component V^S is homogeneous in the sense that the normal component of V^S is zero on the boundary and is totally tangential to the boundary. The curl-free component V^I is homogenous in the sense that the tangential component of V^I vanishes on the boundary and is exactly normal to the boundary. If these Neuman boundary conditions for vector fields are satisfied, then fewer scalar projections are required. A complete summary of work since these early days related to vector tomography can be found in [35]. For tensor tomography Louis [36] claimed that the reconstruction on a bounded domain has no unique solution, but claimed the solenoidal part can be uniquely determined because it is overdetermined. Recent work of McGraw [60] shows how the decomposition of the tensor field on a bounded domain provides a solenoidal and irrotational component with an addition of a homogeneous component. The generalized Helmholtz decomposition on bounded domain is given by $D_{ij} = \partial_i \phi_j + \varepsilon_{imn}(\partial_m \psi_{nj}) + H_{ij}$, where the harmonic tensor field, $[H_{ij}]$, is both solenoidal and irrotational and typically is of small magnitude [60, 61]. The paper by McGraw [61] gives some visual examples of the decomposition of tensor fields where it is shown that the harmonic component is a constant background of low intensity.

In our work we took the approach of Sharafutdinov [47] and assumed that the tensor field that we are reconstructing is a sufficiently smooth symmetric tensor field which vanishes rapidly at infinity. We recognize that this may be a stretch if applied to medical images such as the heart where there can be sharp contrast at organ boundaries that may produce background artifacts. Our cardiac diffusion tensor field was obtained from an MR imaging experiment and thus may not have a unique decomposition, whereas the numerical phantom of the two spherical surfaces was designed to have a unique decomposition of the solenoidal and irrotational components by constructing the phantom as the sum of a particular solenoidal and irrotational components. For the reconstruction of the cardic diffusion tensor field some of the mismatch between the results and the the original tensor field may be a harmonic tensor field of small magintude. We speculate that the same would be true for the reconstruction of a tensor field on a bounded domain, i.e., using our decomposition and algorithm would result in a non-uniqueness (missing part) of a constant homogeneous background of low intensity.

Work in vector tomography has also shown that if the constant attenuator of the scalar projections is known, then only longitudinal scalar projections in the direction of the projection angle [62] are required to reconstruct the vector field. Later Natterer [63] showed that transverse scalar projections would only be required; however, in practice these measurements can be difficult to acquire. Previously we investigated this for vector [64] and tensor [65] fields by simulating attenuated projections of scalar measurements around one orbit. The results indicated that the elements of the vectors are recovered, whereas components of the tensor field are not fully recovered.

E. X-ray dark field imaging

1) X-ray tensor tomography (XTT)

Of particular interest to us is the application of tensor tomography in X-ray dark-field imaging of fiber orientation in tissue. The X-ray tensor tomography (XTT) method [8, 66] divides the reconstruction of tensor fields into two steps: first to reconstruct coefficients of a Cartesian vector representation at each voxel; and then fit the estimated vector coefficients to an ellipsoidal representation of the second rank tensor at each voxel. The forward model represents the small angle scatter as the discrete supposition of the anisotropic scatter signal, much like the Beer–Lambert model for the X-ray attenuation signal [66]. Vogel et al. [67] formulated the reconstruction of the ellipsoidal representation of the fixed basis set of vectors as a regular inverse problem whereby an iterative reconstruction algorithm is used to estimate vector coefficients constrained by an ellipsoidal function. Iterative approaches have advantages in addition to modeling noise, to provide constraints on the solution. A Bayesian approach adding constraints to XTT was pursued by [68] who proposed a cost function with regularization to iteratively reconstruct simultaneously attenuation, phase, and scatter images (with independent penalty functions) from differential phase contrast acquisitions, without the need of phase retrieval. In our work we performed simulations evaluating the model of [8, 67] with the reconstruction of coefficients for a fixed basis set of 7 vectors. The coefficients were reconstructed from Moiré fringe analysis of single-exposure dark field projections obtained from X-ray bi-prism interferometry [69]. Wieczorek et al. [12] modified the forward model [8, 67] to develop an anisotropic X-ray dark field tomography (AXDT) method by replacing the discretization of the scattering function as a fixed basis set of vectors at each voxel with a spherical harmonic expansion. They demonstrated signific differences in the results between XTT and AXDT in the small angle scatter indicating that the spherical harmonic approach may be a more general representation of the small angle scatter than the tensor approach. Early on a differ forward model was proposed by Bayer et al. [9] where instead of a vector basis expansion; the isotropic scatter contribution, the anisotropic scatter contribution, and the in-plane scatter angel was modeled using a sinusoidal expansion where coefficients were reconstructed from X-ray dark field projections using Talbot-Lau grating interferometry. More recently, Kim et al. [14] proposed the use of a periodic array of multi-circular gratings for Talbot-Lau interferometry instead of linear gratings to capture 2D-omnidirectional X-ray scattering signals within a single projection shot, removing the necessity of rotation of the sample relative to the gradient alignment. In this work vector coefficients were reconstructed following the model of Malecki et al. [8, 66].

2) Reciprocal space representation of X-ray scatter

Other groups investigated the possibility of directly reconstructing a q-vector representation of reciprocal space as a measure of the small angle scatter (SAXS) from direct dark field measurements using X-ray raster scanning [10, 11]. The use of raster scanning to measure small angel X-ray scattering (SAXS) is a valuable imaging technique to obtain which q-vectors are probed for each projection. A virtual tomography axis is presented where projection-dependent rotation matrix describes the relationship between laboratory and sample coordination systems. Schaff et al [13] later investigated the possibility of instead of using raster scanning, using XTT data obtained from Talbot-Lau X-ray grating interferometry to fit models of reciprocal space representation of small angle scatter. Ellipsoids are fit to the reconstructed results. As with the use of spherical harmonics in real space representation of scatter, spherical harmonics were also used for the basis representation of q-vectors in reciprocal-space modeling of small angle scatter from data obtained with X-ray raster scanning [10, 70]. To improve the speed of the reconstruction, a fast iterative backprojection reconstruction algorithm [46] was designed to directly reconstruct elements of a second rank tensor. This was the first tensor tomography approach to directly reconstruct elements of a second rank tensor representation of small angle scatter from dark field projections. The tensor representation of the projections was transverse corresponding to the direction of the sensitivity of the gratings.

3) Scatter as a tensor

In many of these approaches the question arises as to whether sufficient data is obtained to uniquely reconstruct the coefficients of the models used to represent the small angle scatter. We know from our work presented in this paper with that of using a filter backprojection algorithm, 3 orthogonal axes obtaining 6 sets of projections provide 6 independent equations to solve for the 6 unknows of a tensor representation of small angle scatter. However, specific orientation dependence of small angle scatter and the non-linear function of the underlying anisotropic mass distribution brings into question as to whether a tensor representation is a correct model of the anisotropic small angel scatter [15]. Graetz [15] investigated whether two approximative linear tensor models with reduced orientation dependence were applicable models of small angle scatter for grating based X-ray or neutron dark-field tensor tomography. Simulations verified that in using tomographic applications with full sampling over a sphere, these linear tensor models can recover orientations up to a statistical accuracy on the scale of 1°. However, if the tensor representation was reconstructed using only a minimal set of three circular acquisition trajectories, principal orientations for isolated volume elements could still be recovered to a statistical accuracy of 5° to 10°.

F. Magnetic resonance imaging

1) Diffusion tensor magnetic resonance imaging (DT-MRI)

The application of tensor tomography in MR diffusion tensor imaging is more in question as to its applicability since most of MRI acquisition schemes (protocols, pulse sequences) acquire data that directly map Fourier space requiring no tomography, only an inverse 2D or 3D Fourier transform to directly obtain the real space image. Even more changeling is the work in the last two decades in developing better diffusion models for brain tractography – where the brain covers a wide range of spatial scale of anatomy from global structure of white matter fiber tracts to microstructure of axons – that go beyond the tensor representation [71, 72]. Some of these methods are modification of the diffusion tensor model; here we present three examples: 1) Neurite Orientation Dispersion and Density Imaging (NODDI) distinguishes between intracellular, extracellular, and cerebrospinal fluid (CSF) compartments by assuming the diffusion signal is the sum of diffusion signals from multiple compartments [73]. Multi-compartment models are limited in modeling bending and fanning fiber configurations in a voxel and in determining the correct number of compartments [74]. 2) Diffusion Kurtosis imaging (DKI) is another class of methods aimed at using a fiber orientation distribution function (fODF) [75] to estimate a fiber orientation which is important for tractography and connective analysis by way of a diffusion orientation function (dODF). DKI is a statistical measure of the deviation from a Gaussian distribution [which is the assumed distribution for diffusion tensor imaging (DTI)], and thus, DKI provides a significantly more complete characterization of water diffusion and tissue structure. This technique is largely based on the same type of pulse sequences employed for DTI, but DKI requires multishell diffusion MRI (dMRI) at higher b values than those conventionally utilized for DTI analysis. 3) Q-space diffeomorphic reconstruction (QSDR). Other limitations of DTI relate to its inability to independently resolve crossing fibers and sensitivity to partial volume effects (PVE) as in studies using dODF to characterize the diffusion distribution. To overcome these effects, the spin distribution function (SDF) can be obtained from generalized Q-sampling imaging (GQI), where SDF represents the proportion of spins undergoing diffusion in different orientations. Notice this is like the case with developing models of X-ray small angle scatter, investigation of reciprocal space to obtain a q-space representations of small angle scatter in tissue as a better model of small angle scatter than a tensor representation. Q-space diffeomorphic reconstruction calculates the transformed SDFs in any given deformation field that satisfies diffeomorphism. To overcome some of these problems Karimi et al [71] proposed to learn a direct mapping between the diffusion measurements in the q-space and the target fODF by using deep neural networks to learn the relationship between the DW-MRI signal and the fiber orientation distribution. The estimation of an fODF, on the other hand is sensitive to noise and prone to predicting false fibers, while other possible methods such as diffusion spectrum imaging (DSI) require a very large number of measurements that can lead to unrealistic scan times.

2) Diffusion tensor tomography magnetic resonance imaging (DTT-MRI)

Our previous work focused on developing diffusion tensor tomography magnetic resonance imaging (DTT-MRI) for the **heart**; one the most difficult organs to perform MR diffusion tensor imaging (MR-DTI) due to motion and the length of time required to obtain adequate images. For ex vivo samples we have acquired images for up to 12 hours on 3T small animal systems [76]. It can take a long time to acquire an MR diffusion tensor image of the heart with sufficient signal to noise, making it impractical for human imaging, though recent imaging times have significantly improved [19, 77-79]. For this reason, in our previous attempts to measure the heart fiber structure required in constructing mechanical models of the heart, we investigated ways of reducing the number of measurements (pulse repetitions), such as measuring and reconstructing only the principal eigenvectors in order to reduce the acquisition times but to provide some structural information of cardiac fiber structure [80]. With the hope that the heart fiber structure could be specified from its solenoidal tensor field, we also performed simulations of reconstructing solenoidal and irrotational images of a numerical helical heart phantom (representing a section of the mid-ventricular wall of the left ventricle) from scalar Radon projections (note: not X-ray projections) of the phantom [53]. Sampling projections around a single axis, we found Radon projections $\tilde{r}_{\underline{\theta}}^{\underline{\alpha}\,\underline{\alpha}}$, $\tilde{r}_{\underline{\theta}}^{\underline{\alpha}\,\underline{\beta}}$, and $\tilde{r}_{\underline{\theta}}^{\underline{\beta}\,\underline{\beta}}$ were needed for each projection $\underline{\theta}$ to reconstruct the three unknowns in the solenoidal tensor field and Radon projections $\tilde{r}_{\underline{\theta}}^{\underline{\theta}\,\underline{\theta}}$, $\tilde{r}_{\underline{\theta}}^{\underline{\theta}\,\underline{\alpha}}$, and $\tilde{r}_{\underline{\theta}}^{\underline{\theta}\,\underline{\beta}}$ were needed to reconstruct the three unknowns in the irrotational component of the tensor field [53]. In this work, we found that a realistic model of the helical fiber structure of the myocardial tissue specifies a diffusion tensor field for which the first principal vector (the vector associated with the maximum eigenvalue) of the solenoidal component accurately approximates the first principal vector of the diffusion tensor.

G. Summary

The second, third, and fourth rank tensors describe a wide range of physical phenomena with potential imaging applications. Second rank tensors are used to represent diffusivity [81], mechanical stress and strain [82], electromagnetic quantities [83] and physics related to gravity [84]. Third rank tensors have been used to describe the apparent bidirectional reflectance distribution function (BRDF) in face relighting applications [85]. Fourth rank tensors can approximate the diffusivity function from the DW-MRI data guaranteeing the symmetric positive-definite property [75]. Other applications include, X-ray strain imaging of crystals, specifically inverting the transverse ray transform of the projections of the diffraction pattern [51], neutron strain imaging of crystals [51, 86], photoelasticity strain imaging of crystals [87], travel time seismology studying the inner structure of the earth to determine the anisotropic index of refraction of the medium involving the mathematical challenge of determining a symmetric second rank tensor Riemannian metric from its integrals along geodesics [88-90], neutron tomography of magnetic vector fields in bulk materials [91], optical tomography of dielectric tensors [92], tomographical imaging of electrical and magnetic sources in brain and heart [93, 94], and tissue magnetic susceptibility tensor MR imaging [95].

In our previous work we performed simulations evaluating the reconstruction of the coefficients for a fixed basis set of 7 vectors from Moiré fringe analysis of projections of a single-exposure of dark field scatter obtained from X-ray bi-prism interferometry [69]. To obtain a tensor representation would have involved performing a second step of fitting the estimated vector coefficients to an ellipsoidal representation of the tensor at each voxel [8, 67]. In our simulations of this previous work, we used a wave optics approach to simulate the projections; whereas, in the present work we did not simulate a specific imaging modality but evaluated our filtered backprojection algorithm by numerically approximating the projections of a generic numerical tensor field and a diffusion tensor field of an excised human heart. Our future interests involve developing algorithms to directly reconstruct the tensor representation of small angle scatter using X-ray bi-prism interferometry [96]. This interest is heightened by the fact that from the work of [15] it is appropriate to represent small angle scatter as a second rank tensor.

VII. Conclusion

We proposed a new filtered backprojection reconstruction algorithm to reconstruct tensor fields from projections acquired around three axes. Using a tensor field decomposition and Fourier projection theorem, we established relationships between the Fourier transform of the directional X-ray projection measurements and the Fourier transform of the solenoidal and irrotational components of the tensor field. The filters were then derived based on the property of the decomposition being non-irrotational for the directional X-ray transform of the tensor around some axes. Thus, the decomposition of the tensor field into solenoidal and irrotational components provides insight into the development of algorithms for the reconstruction of tensor fields with sufficient samples of directional projections and the necessary orbits for acquisition of the projections of the tensor field.

References

[1] J. Tromp, C. Tape, and Q. Liu, "Seismic tomography, adjoint methods, time reversal and banana-doughnut kernels," *Geophysical Journal International,* vol. 160, no. 1, pp. 195-216, 2005.

[2] F. Hofmann *et al.*, "Nano-scale imaging of the full strain tensor of specific dislocations extracted from a bulk sample," *Physical Review Materials,* vol. 4, no. 1, p. 013801, 2020.

[3] G. P. Paternain, M. Salo, and G. Uhlmann, "Tensor tomography on surfaces," *Inventiones Mathematicae,* vol. 193, no. 1, pp. 229-247, 2013.

[4] A. L. Alexander, J. E. Lee, M. Lazar, and A. S. Field, "Diffusion tensor imaging of the brain," *Neurotherapeutics,* vol. 4, no. 3, pp. 316-329, 2007.

[5] H. Einarsdóttir *et al.*, "Computer-aided diagnosis of pulmonary diseases using x-ray darkfield radiography," *Physics in Medicine and Biology,* vol. 60, no. 24, p. 9253, 2015.

[6] T. Baum *et al.*, "X-ray dark-field vector radiography—a novel technique for osteoporosis imaging," *Journal of Computer Assisted Tomography,* vol. 39, no. 2, pp. 286-289, 2015.

[7] S. T. Taba, T. E. Gureyev, M. Alakhras, S. Lewis, D. Lockie, and P. C. Brennan, "X-ray phase-contrast technology in breast imaging: principles, options, and clinical application," *American Journal of Roentgenology,* vol. 211, no. 1, pp. 133-145, 2018.

[8] A. Malecki *et al.*, "X-ray tensor tomography," *Europhysics Letters,* vol. 105, no. 3, p. 38002, 2014.

[9] F. L. Bayer *et al.*, "Reconstruction of scalar and vectorial components in X-ray dark-field tomography," *Proceedings of the National Academy of Sciences of the United States of America,* vol. 111, no. 35, pp. 12699-704, 2014.

[10] M. Liebi *et al.*, "Nanostructure surveys of macroscopic specimens by small-angle scattering tensor tomography," *Nature,* vol. 527, no. 7578, pp. 349-352, 2015.

[11] F. Schaff *et al.*, "Six-dimensional real and reciprocal space small-angle x-ray scattering tomography," *Nature,* vol. 527, no. 7578, pp. 353-356, 2015.

[12] M. Wieczorek, F. Schaff, F. Pfeiffer, and T. Lasser, "Anisotropic x-ray dark-field tomography: A continuous model and its discretization," *Physical Review Letters,* vol. 117, no. 15, p. 158101, 2016.

[13] F. Schaff, F. Prade, Y. Sharma, M. Bech, and F. Pfeiffer, "Non-iterative directional dark-field tomography," *Scientific Reports,* vol. 7, no. 1, pp. 1-9, 2017.

[14] J. Kim, M. Kagias, F. Marone, and M. Stampanoni, "X-ray scattering tensor tomography with circular gratings," *Applied Physics Letters,* vol. 116, no. 13, p. 134102, 2020.

[15] J. Graetz, "Simulation study towards quantitative X-ray and neutron tensor tomography regarding the validity of linear approximations of dark-field anisotropy," *Scientific Reports,* vol. 11, no. 1, pp. 1-11, 2021.

[16] M. J. Moulton, B. D. Hong, and T. W. Secomb, "Simulation of left ventricular dynamics using a low-order mathematical model," *Cardiovascular Engineering and Technology,* vol. 8, no. 4, pp. 480-494, 2017.

[17] M. Froeling, G. J. Strijkers, A. J. Nederveen, S. A. Chamuleau, and P. R. Luijten, "Diffusion tensor MRI of the heart – In vivo Imaging of myocardial fiber architecture," *Current Cardiovascular Imaging Reports,* vol. 7, no. 7, p. 9276, 2014.

[18] A. Das *et al.*, "The effect of microvascular obstruction on the myocardial microstructure: a

diffusion tensor imaging study," *European Heart Journal-Cardiovascular Imaging,* vol. 22, no. Supplement_1, p. jeaa356. 323, 2021.

[19] S. R. Watson, J. D. Dormer, and B. Fei, "Imaging technologies for cardiac fiber and heart failure: a review," *Heart Failure Reviews,* vol. 23, no. 2, pp. 273-289, 2018.

[20] V. Talman and H. Ruskoaho, "Cardiac fibrosis in myocardial infarction—from repair and remodeling to regeneration," *Cell and Tissue Research,* vol. 365, no. 3, pp. 563-581, 2016.

[21] D. M. Kramer and P. C. Lauterbur, "On the problem of reconstructing images of non-scalar parameters from projections. Application to vector fields," *IEEE Transactions on Nuclear Science,* vol. 26, no. 2, pp. 2674-2677, 1979.

[22] S. J. Norton, "Tomographic reconstruction of 2-D vector fields: application to flow imaging," *Geophysical Journal International,* vol. 97, no. 1, pp. 161-168, 1989.

[23] K. B. Winters and D. Rouseff, "A filtered backprojection method for the tomographic reconstruction of fluid vorticity," *Inverse Problems,* vol. 6, no. 4, p. L33, 1990.

[24] H. Braun and A. Hauck, "Tomographic reconstruction of vector fields," *IEEE Transactions on Signal Processing,* vol. 39, no. 2, pp. 464-471, 1991.

[25] S. J. Norton, "Unique tomographic reconstruction of vector fields using boundary data," *IEEE Transactions on Image Processing,* vol. 1, no. 3, pp. 406-412, 1992.

[26] S. Juhlin, "Doppler tomography," in *Proceedings of the 15th Annual International Conference of the IEEE Engineering in Medicine and Biology Societ*, 1993, pp. 212-213: IEEE.

[27] G. Sparr, K. Strahlen, K. Lindstrom, and H. W. Persson, "Doppler tomography for vector fields," *Inverse Problems,* vol. 11, no. 5, p. 1051, 1995.

[28] A. Denisov, A. Popov, and V. Sterlyadkin, "Doppler tomography problem for a two-dimensional vector field," *Moscow University Computational Mathematics Cybernetics,* vol. 1, pp. 17-20, 1995.

[29] L. Desbat and A. Wernsdorfer, "Direct algebraic reconstruction and optimal sampling in vector field tomography," *IEEE Transactions on Signal Processing,* vol. 43, no. 8, pp. 1798-1808, 1995.

[30] J. L. Prince, "Convolution backprojection formulas for 3-D vector tomography with application to MRI," *IEEE Transactions on Image Processing,* vol. 5, no. 10, pp. 1462-1472, 1996.

[31] G. Sparr and K. Stråhlén, "Vector field tomography: an overview," *IMA Volumes in Mathematics its Applications Computational Radiology Imaging: Therapy and Diagnostic,* vol. 110, 1998.

[32] T. Schuster, "The 3D Doppler transform: elementary properties and computation of reconstruction kernels," *Inverse Problems,* vol. 16, no. 3, pp. 701-723, 2000.

[33] T. Schuster, "An efficient mollifier method for three-dimensional vector tomography: convergence analysis and implementation," *Inverse Problems,* vol. 17, no. 4, pp. 739-766, 2001.

[34] V. Sharafutdinov, "Slice-by-slice reconstruction algorithm for vector tomography with incomplete data," *Inverse Problems,* vol. 23, no. 6, p. 2603, 2007.

[35] T. Schuster, *Mathematical methods in biomedical imaging and intensity-modulated radiation therapy (IMRT)*. volume 7 of Publications of the Scuola Normale Superiore, CRM Series, 20 Years of imaging in vector field tomography: a review, 2008.

[36] A. K. Louis, S. V. Maltseva, A. P. Polyakova, T. Schuster, and I. E. Svetov, "On solving the slice-by-slice three-dimensional 2-tensor tomography problems using the approximate inverse method," *Journal of Physics Conference Series,* vol. 1715, no. 1, p. 012036, 2021.

[37] G. T. Gullberg, R. D. Ghosh, G. L. Zeng, A. Alexander, and D. Parker, "Tensor tomography," *IEEE Transactions on Nuclear Science,* vol. 46, no. 4, pp. 991-1000, 1999.

[38] G. Gullberg and M. Defrise, "Three-dimensional tomography for vector and tensor fields," in *Proceedings of the 1999 International Meeting on Fully Three-Dimensional Image Reconstruction in Radiology and Nuclear Medicine*, 1999, pp. 369-372.

[39] G. Gullberg, M. Defrise, V. Panin, and G. Zeng, "Backprojection filtering algorithms for reconstruction of vector and second order tensor fields," in *2000 IEEE Nuclear Science Symposium. Conference Record (Cat. No. 00CH37149)*, 2000, vol. 2, pp. 15/277-15/281 vol. 2: IEEE.

[40] M. Defrise and G. T. Gullberg, "3D reconstruction of tensors and vectors," *Office of Scientific & Technical Information Technical Reports,* 2005.

[41] A. Denisjuk, "Inversion of the x-ray transform for 3D symmetric tensor fields with sources on a curve," *Inverse Problems,* vol. 22, no. 2, pp. 399-411, 2006.

[42] W. Lionheart and V. Sharafutdinov, "Reconstruction algorithm for the linearized polarization tomography problem with incomplete data," *Contemporary Mathematics,* vol. 14, p. 137, 2009.

[43] N. M. Desai and W. Lionheart, "An explicit reconstruction algorithm for the transverse ray transform of a second rank tensor field from three axis data," *Inverse Problems,* vol. 32, no. 11, p. 115009, 2016.

[44] E. Y. Derevtsov, A. Louis, S. Maltseva, A. Polyakova, and I. Svetov, "Numerical solvers based on the method of approximate inverse for 2D vector and

2-tensor tomography problems," *Inverse Problems,* vol. 33, no. 12, p. 124001, 2017.

[45] R. Bammer, S. J. Holdsworth, W. B. Veldhuis, and S. T. Skare, "New methods in diffusion-weighted and diffusion tensor imaging," *Magnetic Resonance Imaging Clinics of North America,* vol. 17, no. 2, pp. 175-204, 2009.

[46] Z. Gao, M. Guizar-Sicairos, V. Lutz-Bueno, A. Schrter, and M. Georgiadis, "High-speed tensor tomography: iterative reconstruction tensor tomography (IRTT) algorithm," *Acta Crystallographica,* vol. 75, no. 2, pp. 223-238, 2019.

[47] V. A. Sharafutdinov, "Integral geometry of tensor fields," *Inverse and Ill-posed Problems Series,* 1994.

[48] G. R. Wang, "A Cramer rule for minimum-norm (T) least-squares (S) solution of inconsistent linear equations," *Linear Algebra & Its Applications,* vol. 74, pp. 213-218, 1986.

[49] H. Stark, J. Woods, I. Paul, and R. Hingorani, "Direct Fourier reconstruction in computer tomography," *IEEE Transactions on Acoustics, Speech, and Signal Processing,* vol. 29, no. 2, pp. 237-245, 1981.

[50] D. Rohmer, A. Sitek, and G. T. Gullberg, "Reconstruction and visualization of fiber and laminar structure in the normal human heart from ex vivo DTMRI data," *Investigative Radiology,* vol. 42, no. 11, pp. 777-789, 2007.

[51] W. Lionheart and P. J. Withers, "Diffraction tomography of strain," *Inverse Problems,* vol. 31, no. 4, p. 045005, 2015.

[52] P. B. Kingsley, "Introduction to diffusion tensor imaging mathematics: Part III. Tensor calculation, noise, simulations, and optimization," *Concepts in Magnetic Resonance Part A,* vol. 28A, no. 2, pp. 155-179, 2006.

[53] G. T. Gullberg, M. Defrise, V. Y. Panin, and G. L. Zeng, "Efficient cardiac diffusion tensor MRI by three-dimensional reconstruction of solenoidal tensor fields," *Magnetic Resonance Imaging,* vol. 19, no. 2, pp. 233-256, 2001.

[54] E. Y. Derevtsov and I. Svetov, "Tomography of tensor fields in the plain," *Eurasian Journal of Mathematical and Computer Applications,* vol. 3, no. 2, pp. 24-68, 2015.

[55] A. Polyakova and B. Hahn, "A solution of the dynamic two-dimensional 2-tensor tomography problem using the SVD-method," *Frontier in Mathematics Computer Science,* vol. 12, p. 82, 2020.

[56] A. K. Louis and P. Maass, "A mollifier method for linear operator equations of the first kind," *Inverse Problems,* vol. 6, no. 3, p. 427, 1990.

[57] G. B. Arfken and H.-J. Weber, *Mathematical methods for physicists*. Academic Press Harcourt Brace Jovanovich, San Diego, 1967.

[58] A. Polyakova and I. Svetov, "The singular value decomposition of the dynamic ray transforms operators acting on 2-tensor fields in ℝ2," in *Journal of Physics: Conference Series*, 2021, vol. 1715, no. 1, p. 012040: IOP Publishing.

[59] N. F. Osman and J. L. Prince, "3D vector tomography on bounded domains," *Inverse Problems,* vol. 14, no. 1, p. 185, 1998.

[60] T. McGraw, T. Kawai, I. Yassine, and L. Zhu, "New scalar measures for diffusion-weighted MRI visualization," in *International Symposium on Visual Computing*, 2009, pp. 934-943: Springer.

[61] T. McGraw, T. Kawai, I. Yassine, and L. Zhu, "Visualizing high-order symmetric tensor field structure with differential operators," *Journal of Applied Mathematics,* vol. 2011, pp. 327-350, 2011.

[62] A. A. Bukhgeim and S. G. Kazantsev, "Full Reconstruction of a Vector Field from Its Attenuated Vectorial Radon Transform," in *Modelling, Identification and Control*, 2003, pp. 294-298.

[63] F. Natterer, "Inverting the attenuated vectorial Radon transform," *Inverse Ill-Posed Problems,* vol. 13, no. 1, pp. 93-101, 2005.

[64] Q. Huang, "Attenuated vector tomography--An approach to image flow vector fields with doppler ultrasonic imaging," 2008.

[65] Q. Huang and G. T. Gullberg, "Attenuation corrected tensor tomography-attenuation helps in the case of insufficient measurements," in *2007 IEEE Nuclear Science Symposium Conference Record*, 2007, vol. 6, pp. 4103-4109: IEEE.

[66] A. Malecki, "X-ray tensor tomography," 2014. PhD thesis, Technical University of München

[67] J. Vogel *et al.*, "Constrained x-ray tensor tomography reconstruction," *Optics Express,* vol. 23, no. 12, pp. 15134-15151, 2015.

[68] B. Brendel, M. von Teuffenbach, P. B. Noël, F. Pfeiffer, and T. Koehler, "Penalized maximum likelihood reconstruction for x-ray differential phase - contrast tomography," *Medical physics,* vol. 43, no. 1, pp. 188-194, 2016.

[69] W. Tao *et al.*, "Tomography of dark - field scatter including single - exposure Moiré fringe analysis with X - ray biprism interferometry—A simulation study," *Medical Physics,* vol. 48, no. 10, pp. 6293-6311, 2021.

[70] M. Liebi *et al.*, "Small-angle x-ray scattering tensor tomography: model of the three-dimensional reciprocal-space map, reconstruction algorithm and angular sampling requirements," *Acta Crystallographica Section A: Foundations and Advances,* vol. 74, no. 1, pp. 12-24, 2018.

[71] D. Karimi, L. Vasung, C. Jaimes, F. Machado-Rivas, S. K. Warfield, and A. Gholipour, "Learning to estimate the fiber orientation distribution function

from diffusion-weighted MRI," *NeuroImage,* vol. 239, p. 118316, 2021.

[72] Y. Masutani, "Recent advances in parameter inference for diffusion MRI signal models," *Magnetic Resonance in Medical Sciences,* pp. rev. 2021-0005, 2021.

[73] M. Bergamino, E. G. Keeling, V. R. Mishra, A. M. Stokes, and R. R. Walsh, "Assessing white matter pathology in early-stage Parkinson disease using diffusion MRI: a systematic review," *Frontiers in neurology,* p. 314, 2020.

[74] B. Jeurissen, A. Leemans, J. D. Tournier, D. K. Jones, and J. Sijbers, "Investigating the prevalence of complex fiber configurations in white matter tissue with diffusion magnetic resonance imaging," *Human Brain Mapping,* vol. 34, no. 11, pp. 2747-2766, 2013.

[75] A. Barmpoutis, M. S. Hwang, D. Howland, J. R. Forder, and B. C. Vemuri, "Regularized positive-definite fourth order tensor field estimation from DW-MRI," *NeuroImage,* vol. 45, no. 1, pp. S153-S162, 2009.

[76] N. Tran, A. Giannakidis, G. T. Gullberg, and Y. Seo, "Quantitative analysis of hypertrophic myocardium using diffusion tensor magnetic resonance imaging," *Journal of Medical Imaging,* vol. 3, no. 4, p. 046001, 2016.

[77] S. Nielles‐Vallespin, A. Scott, P. Ferreira, Z. Khalique, D. Pennell, and D. Firmin, "Cardiac diffusion: technique and practical applications," *Journal of Magnetic Resonance Imaging,* vol. 52, no. 2, pp. 348-368, 2020.

[78] Z. Khalique, P. F. Ferreira, A. D. Scott, S. Nielles-Vallespin, D. N. Firmin, and D. J. Pennell, "Diffusion tensor cardiovascular magnetic resonance imaging: a clinical perspective," *JACC: Cardiovascular Imaging,* vol. 13, no. 5, pp. 1235-1255, 2020.

[79] S. Paddock *et al.*, "Clinical translation of three-dimensional scar, diffusion tensor imaging, four-Dimensional flow, and quantitative perfusion in cardiac MRI: A comprehensive review," *Frontiers in Cardiovascular Medicine,* vol. 8, p. 670, 2021.

[80] V. Y. Panin, G. L. Zeng, M. Defrise, and G. T. Gullberg, "Diffusion tensor MR imaging of principal directions: a tensor tomography approach," *Physics in Medicine Biology,* vol. 47, no. 15, p. 2737, 2002.

[81] E. Özarslan and T. H. Mareci, "Generalized diffusion tensor imaging and analytical relationships between diffusion tensor imaging and high angular resolution diffusion imaging," *Magnetic Resonance in Medicine,* vol. 50, no. 5, pp. 955-965, 2003.

[82] T. Chung, *Applied continuum mechanics*. Cambridge University Press, 1996.

[83] A. Kovetz, *Electromagnetic Theory*. Oxford University Press Oxford, 2000.

[84] S. M. Carroll, "An introduction to general relativity: spacetime and geometry," *Addison Wesley,* vol. 101, p. 102, 2004.

[85] R. Kumar, A. Barmpoutis, A. Banerjee, and B. C. Vemuri, "Non-Lambertian reflectance modeling and shape recovery of faces using tensor splines," *IEEE Transactions on Pattern Analysis Machine Intelligence,* vol. 33, no. 3, pp. 533-567, 2010.

[86] B. Abbey, S. Y. Zhang, W. Vorster, and A. M. Korsunsky, "Reconstruction of axisymmetric strain distributions via neutron strain tomography," *Nuclear Instruments Methods in Physics Research Section B,* vol. 270, pp. 28-35, 2012.

[87] D. D. Karov and A. E. Puro, "Tensor tomography of stresses in cubic single crystals," *Petersburg Polytechnical University Journal: Physics and Mathematics,* vol. 1, no. 1, pp. 24-28, 2015.

[88] M. Salo and G. Uhlmann, "The attenuated ray transform on simple surfaces," *Journal of Differential Geometry,* vol. 88, no. 1, pp. 161-187, 2011.

[89] G. P. Paternain, M. Salo, and G. Uhlmann, "Tensor tomography: progress and challenges," 2013.

[90] P. Stefanov, G. Uhlmann, A. Vasy, and H. Zhou, "Travel time tomography," *Acta Mathematica Sinica, English Series,* vol. 35, no. 6, pp. 1085-1114, 2019.

[91] A. Hilger, I. Manke, N. Kardjilov, M. Osenberg, H. Markötter, and J. Banhart, "Tensorial neutron tomography of three-dimensional magnetic vector fields in bulk materials," *Nature Communications,* vol. 9, no. 1, pp. 1-7, 2018.

[92] H. Hammer and W. R. Lionheart, "Reconstruction of spatially inhomogeneous dielectric tensors through optical tomography," *Journal of the Optical Society of America A,* vol. 22, no. 2, pp. 250-255, 2005.

[93] D. S. Tuch, V. J. Wedeen, A. M. Dale, J. S. George, and J. W. Belliveau, "Conductivity tensor mapping of the human brain using diffusion tensor MRI," *Proceedings of the National Academy of Sciences,* vol. 98, no. 20, pp. 11697-11701, 2001.

[94] Z. Hu, K. Ye, M. Bai, Z. Yang, and Q. Lin, "Solving the magnetocardiography forward problem in a realistic three-dimensional heart-torso model," *IEEE Access,* vol. 9, pp. 107095-107103, 2021.

[95] D. Pavlovic, S. Pekic, M. Stojanovic, and V. Popovic, "Traumatic brain injury: neuropathological, neurocognitive and neurobehavioral sequelae," *Pituitary,* vol. 22, no. 3, pp. 270-282, 2019.

[96] G. T. Gullberg, U. Shrestha, S. J. W. Kim, Y. Seo, and M. Fuller, "X‐ray bi‐prism interferometry—A design study of proposed novel hardware," *Medical Physics,* vol. 48, no. 10, pp. 6508-6523, 2021.

Appendix. Tensor field decomposition

It was shown by Sharafutdinov [47], that a smooth symmetric tensor field which vanishes rapidly at infinity can be decomposed in a unique way as $t_{ij} = t_{ij}^S(\underline{x}) + \frac{1}{2}\left(\partial_i \phi_j(\underline{x}) + \partial_j \phi_i(\underline{x})\right)$, where $\underline{\phi}(\underline{x})$ is a vector potential that yields a curl free irrotational tensor field and $t_{ij}^S(\underline{x})$ is a symmetric solenoidal tensor field, which is divergence free: $\sum_i \partial_i t_{ij}^S(\underline{x}) = \sum_j \partial_j t_{ij}^S(\underline{x}) = 0$. If we take the Fourier transform, we see that $\sum_i \sigma_i \tilde{t}_{ij}^S(\underline{\sigma}) = \sum_j \sigma_j \tilde{t}_{ij}^S(\underline{\sigma}) = 0$.

In our paper we considered a similar decomposition, but explicitly specify the solenoidal component as a curl of a tensor potential as is done in the Helmholz vector field decomposition with a vector potential. We consider the following decomposition of a symmetric tensor field T:

$$T(\underline{x}) = T_\Psi^S(\underline{x}) + T_\Phi^I(\underline{x})$$

where the solenoidal component $T_\Psi^S(\underline{x})$ is a symmetric tensor and is divergence free and $T_\Phi^I(\underline{x})$ is a curl free symmetric tensor. We write the solenoidal component as $T_\Psi^S(\underline{x}) = \nabla \times \Psi(\underline{x})$, where

$$\Psi(\underline{x}) = \begin{bmatrix} \Psi_{xx} & \Psi_{xy} & \Psi_{xz} \\ \Psi_{yx} & \Psi_{yy} & \Psi_{yz} \\ \Psi_{zx} & \Psi_{zy} & \Psi_{zz} \end{bmatrix}(\underline{x}) .$$

A correct interpretation of the curl of a second rank tensor is the vector curl operation applied to each column of Ψ, whereas the formal definition of the curl of a second rank tensor is [37, 61]

$$\nabla \times \Psi(\underline{x}) = \begin{bmatrix} \frac{\partial \Psi_{zx}}{\partial y} - \frac{\partial \Psi_{yx}}{\partial z} & \frac{\partial \Psi_{zy}}{\partial y} - \frac{\partial \Psi_{yy}}{\partial z} & \frac{\partial \Psi_{zz}}{\partial y} - \frac{\partial \Psi_{yz}}{\partial z} \\ \frac{\partial \Psi_{xx}}{\partial z} - \frac{\partial \Psi_{zx}}{\partial x} & \frac{\partial \Psi_{xy}}{\partial z} - \frac{\partial \Psi_{zy}}{\partial x} & \frac{\partial \Psi_{xz}}{\partial z} - \frac{\partial \Psi_{zz}}{\partial x} \\ \frac{\partial \Psi_{yx}}{\partial x} - \frac{\partial \Psi_{xx}}{\partial y} & \frac{\partial \Psi_{yy}}{\partial x} - \frac{\partial \Psi_{xy}}{\partial y} & \frac{\partial \Psi_{yz}}{\partial x} - \frac{\partial \Psi_{xz}}{\partial y} \end{bmatrix}(\underline{x}) ,$$

with elements defined by

$$t_{kl} = \sum_{i=1}^{3} \sum_{j=1}^{3} \nabla_i \Psi_{jl} \epsilon_{ijk} \quad ,$$

where ε_{ijk} is the permutation tensor (Levi-Civita symbols):

$$\varepsilon_{ijk} = \begin{cases} +1 \ (i,j,k) \text{ is an even permutation of indices} \\ -1 \ (i,j,k) \text{ is an odd permutation of indices} \\ \qquad 0 \text{ otherwise} \end{cases}$$

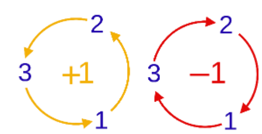

Next take the Fourier transform of $\nabla \times \Psi(\underline{x})$

$$\widetilde{\nabla \times \Psi}(\underline{\sigma}) = \begin{bmatrix} \sigma_y \tilde{\Psi}_{zx} - \sigma_z \tilde{\Psi}_{yx} & \sigma_y \tilde{\Psi}_{zy} - \sigma_z \tilde{\Psi}_{yy} & \sigma_y \tilde{\Psi}_{zz} - \sigma_z \tilde{\Psi}_{yz} \\ \sigma_z \tilde{\Psi}_{xx} - \sigma_x \tilde{\Psi}_{zx} & \sigma_z \tilde{\Psi}_{xy} - \sigma_x \tilde{\Psi}_{zy} & \sigma_z \tilde{\Psi}_{xz} - \sigma_x \tilde{\Psi}_{zz} \\ \sigma_x \tilde{\Psi}_{yx} - \sigma_y \tilde{\Psi}_{xx} & \sigma_x \tilde{\Psi}_{yy} - \sigma_y \tilde{\Psi}_{xy} & \sigma_x \tilde{\Psi}_{yz} - \sigma_y \tilde{\Psi}_{xz} \end{bmatrix}(\underline{\sigma}) .$$

Divergence free: $\sum_i \partial_i t_{ij}^S(\underline{x}) = \sum_j \partial_j t_{ij}^S(\underline{x}) = 0$ implies $\sum_i \sigma_i \tilde{t}_{ij}^S(\underline{\sigma}) = \sum_j \sigma_j \tilde{t}_{ij}^S(\underline{\sigma}) = 0$ thus

$$\begin{gathered} \sigma_x[\sigma_y \tilde{\Psi}_{zx} - \sigma_z \tilde{\Psi}_{yx}] + \sigma_y[\sigma_z \tilde{\Psi}_{xx} - \sigma_x \tilde{\Psi}_{zx}] + \sigma_z[\sigma_x \tilde{\Psi}_{yx} - \sigma_y \tilde{\Psi}_{xx}] = 0 \\ \Rightarrow [\sigma_y \sigma_z - \sigma_y \sigma_z] \tilde{\Psi}_{xx} = 0 \\ \sigma_x[\sigma_y \tilde{\Psi}_{zy} - \sigma_z \tilde{\Psi}_{yy}] + \sigma_y[\sigma_z \tilde{\Psi}_{xy} - \sigma_x \tilde{\Psi}_{zy}] + \sigma_z[\sigma_x \tilde{\Psi}_{yy} - \sigma_y \tilde{\Psi}_{xy}] = 0 \\ \Rightarrow [\sigma_z \sigma_x - \sigma_x \sigma_z] \tilde{\Psi}_{yy} = 0 \\ \sigma_x[\sigma_y \tilde{\Psi}_{zz} - \sigma_z \tilde{\Psi}_{yz}] + \sigma_y[\sigma_z \tilde{\Psi}_{xz} - \sigma_x \tilde{\Psi}_{zz}] + \sigma_z[\sigma_x \tilde{\Psi}_{yz} - \sigma_y \tilde{\Psi}_{xz}] = 0 \\ \Rightarrow [\sigma_x \sigma_y - \sigma_y \sigma_x] \tilde{\Psi}_{zz} = 0 \end{gathered}$$

If we choose $\tilde{\Psi}_{xx} = \tilde{\Psi}_{yy} = \tilde{\Psi}_{zz} = 0$ and $\widetilde{\nabla \times \Psi}(\underline{\sigma})$ is a symmtric tensor then

$$-\sigma_x \tilde{\Psi}_{zx} = \sigma_y \tilde{\Psi}_{zy} \Rightarrow \tilde{\Psi}_{zx} = -\frac{\sigma_y}{\sigma_x}\tilde{\Psi}_{zy}$$
$$\sigma_x \tilde{\Psi}_{yx} = -\sigma_z \tilde{\Psi}_{yz} \Rightarrow \tilde{\Psi}_{yx} = -\frac{\sigma_z}{\sigma_x}\tilde{\Psi}_{yz}$$
$$-\sigma_y \tilde{\Psi}_{xy} = \sigma_z \tilde{\Psi}_{xz} \Rightarrow \tilde{\Psi}_{xy} = -\frac{\sigma_z}{\sigma_y}\tilde{\Psi}_{xz}$$

Choose $\tilde{\Psi}_{xz}=-\sigma_y \tilde{X}_1$, $\tilde{\Psi}_{yz} = \sigma_x \tilde{X}_2$, $\tilde{\Psi}_{zy} = -\sigma_x \tilde{X}_3$, then

$$-\sigma_x \tilde{\Psi}_{zx} = \sigma_y \tilde{\Psi}_{zy} \Rightarrow \tilde{\Psi}_{zx} = -\frac{\sigma_y}{\sigma_x}\left(-\sigma_x \tilde{X}_3\right)$$
$$\sigma_x \tilde{\Psi}_{yx} = -\sigma_z \tilde{\Psi}_{yz} \Rightarrow \tilde{\Psi}_{yx} = -\frac{\sigma_z}{\sigma_x}\left(\sigma_x \tilde{X}_2\right)$$
$$-\sigma_y \tilde{\Psi}_{xy} = \sigma_z \tilde{\Psi}_{xz} \Rightarrow \tilde{\Psi}_{xy} = -\frac{\sigma_z}{\sigma_y}\left(-\sigma_y \tilde{X}_1\right)$$

$$\tilde{\Psi}_{zx} = -\frac{\sigma_y}{\sigma_x}\left(-\sigma_x \tilde{X}_3\right) = \sigma_y \tilde{X}_3$$
$$\tilde{\Psi}_{yx} = -\frac{\sigma_z}{\sigma_x}\left(-\sigma_x \tilde{X}_2\right) = -\sigma_z \tilde{X}_2$$
$$\tilde{\Psi}_{xy} = -\frac{\sigma_z}{\sigma_y}\left(-\sigma_y \tilde{X}_1\right) = \sigma_z \tilde{X}_1$$

With $\tilde{\Psi}_{xx} = \tilde{\Psi}_{yy} = \tilde{\Psi}_{zz} = 0$ and taking the inverse Fourier transform of the elements $\tilde{\Psi}_{ab}$, we have

$$\Psi(\underline{x}) = \begin{bmatrix} 0 & \frac{\partial X_1}{\partial z} & -\frac{\partial X_1}{\partial y} \\ -\frac{\partial X_2}{\partial z} & 0 & \frac{\partial X_2}{\partial x} \\ \frac{\partial X_3}{\partial y} & -\frac{\partial X_3}{\partial x} & 0 \end{bmatrix}(\underline{x}) \,,$$

and

$$T_{\Psi}^{S}(\underline{x}) = \nabla \times \Psi(\underline{x}) = \begin{bmatrix} \frac{\partial^2 X_3}{\partial y^2} + \frac{\partial^2 X_2}{\partial z^2} & -\frac{\partial^2 X_3}{\partial y \partial x} & -\frac{\partial^2 X_2}{\partial z \partial x} \\ -\frac{\partial^2 X_3}{\partial x \partial y} & \frac{\partial^2 X_1}{\partial z^2} + \frac{\partial^2 X_3}{\partial x^2} & -\frac{\partial^2 X_1}{\partial z \partial y} \\ -\frac{\partial^2 X_2}{\partial x \partial z} & -\frac{\partial^2 X_1}{\partial y \partial z} & \frac{\partial^2 X_2}{\partial x^2} + \frac{\partial^2 X_1}{\partial y^2} \end{bmatrix}(\underline{x})$$

Note that $T_{\Psi}^{S}(\underline{x})$ is a symmetric divergence free tensor: $\sum_i \partial_i t_{ij}^{S}(\underline{x}) = \sum_j \partial_j t_{ij}^{S}(\underline{x}) = 0$, for example

$$\frac{\partial}{\partial x}\left[\frac{\partial^2 X_3}{\partial y^2} + \frac{\partial^2 X_2}{\partial z^2}\right] - \frac{\partial}{\partial y}\frac{\partial^2 X_3}{\partial y \partial x} - \frac{\partial}{\partial z}\frac{\partial^2 X_2}{\partial z \partial x} = \frac{\partial^3 X_3}{\partial x \partial y^2} + \frac{\partial^3 X_2}{\partial x \partial z^2} - \frac{\partial^3 X_3}{\partial y^2 \partial x} - \frac{\partial^3 X_2}{\partial z^2 \partial x} = 0\,.$$